Ultra-fast optical signal encoding and analysis for communications and data fusion networks

Final Technical Report

AFOSR Grant Number
F49620-96-1-0163

1 May 2000

20000601 091

REPORT DOCUMENTATION PAGE

AFRL-SR-BL-TR-00-

0793

maintaining gestions for the Office of

1. AGENCY USE ONLY (Leave blank)	2. REPORT DATE 5/1/2000	3. REPORT TYPE AND DATES COVERED Final 4/1/96-3/31/99

4. TITLE AND SUBTITLE	5. FUNDING NUMBERS
Ultra-fast optical signal encoding and analysis for communications and data fusion networks	F49620-96-1-0163

6. AUTHOR(S)

David J. Brady, James J. Coleman and Kenneth G. Purchase

7. PERFORMING ORGANIZATION NAME(S) AND ADDRESS(ES)	8. PERFORMING ORGANIZATION REPORT NUMBER
Department of Electrical and Computer Engineering University of Illinois Urbana, Illinois 61801	

9. SPONSORING / MONITORING AGENCY NAME(S) AND ADDRESS(ES)	10. SPONSORING / MONITORING AGENCY REPORT NUMBER
Dr.Kent Miller AFOSR/NE 801 North Randolph Street, Room 732 Arlington, Virginia 22203-1977	

11. SUPPLEMENTARY NOTES

12a. DISTRIBUTION / AVAILABILITY STATEMENT	12b. DISTRIBUTION CODE
Approved for public release, distribution unlimited	

13. ABSTRACT *(Maximum 200 Words)*

We describe the distributed Bragg pulse shaper, the quantum dot spectrometer and interferometric imaging systems developed under this program. The distributed Bragg pulse shaper is a series of partially reflecting Bragg mirrors constructed over an integrated optical waveguide. Through parallel electrical modulation of the Bragg mirror resonances one can encode terahertz bandwidth optical signals with this device. Quantum dot detectors and interferometric sensors provide complementary technologies for detecting such signals. Quantum dot spectrometers combine the spectral discrimination of quantum confined absorption with resonant tunneling for channel isolation. Interferometric systems map spectral or temporal signal features onto spatially separate channels. In this sense, interferometry acts as a serial-to-parallel complement to the parallel-to-serial action of the pulse shaper.

14. SUBJECT TERMS			15. NUMBER OF PAGES
			16. PRICE CODE

17. SECURITY CLASSIFICATION OF REPORT	18. SECURITY CLASSIFICATION OF THIS PAGE	19. SECURITY CLASSIFICATION OF ABSTRACT	20. LIMITATION OF ABSTRACT

TABLE OF CONTENTS

Executive Summary

The goal of this program was to develop pulse shapers for terahertz bandwidth signal encoding and to develop sensor systems capable of detecting and analyzing such signals. These technologies are critical for future very high speed communications and sensing networks.This program produced significant progress in the development of

1. Distributed Bragg pulse shapers. The distributed Bragg pulse shaper is a serial terahertz time, spectral or coherence domain signal encoder. The pulse shaper functions a parallel access serial output encoder. The DBPS was invented and developed under this program. Terahertz packet encoding was successfully demonstrated in GaAs DBPS devices.
2. Quantum dot materials and detectors. Compact, efficient and fast sensors are needed for extremely high speed or broadband systems. Quantum dot detectors combine spectral resolution comparable to rare earth materials with electronic response. Several designs and implementations of quantum dot detectors were completed and quantum dot liquid phase self-organizing dot materials growth was established.
3. Interferometric detection and imaging systems. Interferometric sensors provide an alternative or complementary path to ultra-fast and broadband sensors. Interferometric approaches may be used with conventional or quantum dot devices. We explored signal and noise constraints in interferometric systems and developed links between interferometric communications sensors and imaging systems.

Results under (3) for data fusion applications were particularly dramatic. Work in this area continues under the AFOSR program "Distributed optoelectronic processing for multidimensional digital imaging." Work under (2) led to potentially revolutionary materials and receiver architectures. Work in this area continues under DARPA support. Specific results under these three areas are summarized below.

The following personnel worked on this program:

- Co-PIs: David J. Brady and James J. Coleman
- Staff: John Hughes
- Postdoctoral Associates: Dr. Jose Jiminez (under Beckman Institute Support, now at Nanotronics) Dr. Hai Lin, Dr. George Barbastathis (now at MIT).
- Graduate Students:
  o Dr. K. G. Purchase, now at Lightwave Microsystems, Mountain View, CA
  o Dr. K. B. Hill, now at Montana State University
  o Dr. J.P. Guo, now at Rockwell International
  o Dr. Gary Smith, now at Lasertron
  o Dr. S. David Roh, now at Agilent Technologies
  o Dr. Mark Osowski, now at Lucent Technologies
  o Dr. R. M. Lammert, now at Lucent Technolgoies
  o R. A. Stack, now academic staff, University of Illinois
  o Remy Tumbar, Ph. D. expected fall 2000, University of Illinois
  o T. S. Yeoh, Ph. D. candidate, University of Illinois
  o Colin Byrne, now at Display Tech

Papers and theses derived partially or completely from this program include:

- Scott Alan Basinger, "Space-time imaging and interferometric microscopy," Ph. D. Thesis, University of Illinois at Urbana-Champaign, 1996.
- Kenneth Graham Purchase, "Distributed Bragg pulse shapers for terahertz modulation and ultrafast communications," Ph. D. Thesis, University of Illinois at Urbana-Champaign, 1998.
- Junpeng Guo, "Holographic and polarization methods for optical field analysis," Ph. D. Thesis, University of Illinois at Urbana-Champaign, 1998.
- Ronald A. Stack, "Nanopositioning and superresolved microscopy using multichannel interferometric cross correlators," M.S. Thesis, University of Illinois at Urbana-Champaign, 1997.
- Kent B. Hill, Scott A. Basinger, Ronald A. Stack and David J. Brady, "Noise and information in interferometric cross correlators," *Applied Optics*, 36, 3948-58, (1997).
- J. L. Jimenez, L. R. C. Fonseca, D. J. Brady, J. P. Leburton, D. E. Wohlert, and K. Y. Cheng, "The quantum dot spectrometer," Applied Physics Letters, 71, 3558-3560, (1997).
- Scott A. Basinger, Ronald A. Stack, Kent B. Hill and David J. Brady, "Superresolved optical scanning using polychromatic light," *Journal of the Optical Society of America A*, 14, 3242-3250 (1997).
- D. L. Marks and D. J. Brady, "Three-dimensional coherence imaging in the Fresnel domain," Applied Optics, 38, 1332-1342(1999).
- K. G. Purchase, D. J. Brady, S. D. Roh, R. M. Lammert, M. L. Osowski, J. J. Coleman, and J. S. Hughes, "The distributed Bragg pulse shaper," Journal of Lightwave Technology, 17, 621-628(1999).
- T. S. Yeoh, C. P. Liu, R. B. Swint, S. D. Roh, K. E. Lee, J. J. Coleman, A. Mitofsky and S. G. Bishop, "Fully coherent self-organized InAs quantum dots grown by atmospheric metalorganic chemical vapor deposition," submitted to Electronic Materials Letters.

Background

Serial communications channels are limited by drive and input electronics to bandwidths of tens of gigahertz to one hundred gigahertz. To overcome this limit, future systems will have to rely on parallel input signals. The goals of this program were to demonstrate the feasibility of a continuous-output modulator that transforms parallel gigahertz frequency electrical signals into a serial terahertz optical signal and to develop compact sensors capable of receiving signals from this modulator.

Ultrafast point-to-point links have been addressed by a number of approaches, including *Wavelength Division Multiplexing* (WDM), *Time Division Multiplexing* (TDM) and *Coherence Domain Multiplexing* (CDM). Wavelength division multiplexing is the most common approach to high-bandwidth communications. In WDM systems, information is transmitted independently on a series of channels, each at a different wavelength. This is usually envisioned with multiple sources, each at a different wavelength. Many companies are now marketing WDM systems capable of combining four or eight channels at up to 10 Gbit/s each. However, systems at above 100 Gbit/s remain too costly for widespread deployment, because of difficulties such as source

wavelength stability and the high costs of multiplexing and demultiplexing large numbers of sources. Also, because pulses at a given wavelength are localized and therefore contain high intensities, relatively wide channel spacing is required to avoid crosstalk between channels due to nonlinear effects in the fiber. In another WDM scheme, sometimes called *frequency slicing*, data is encoded independently in different frequency intervals in a single high-bandwidth source. This technique simplifies source stability issues, but still suffers from difficulties in multiplexing and demultiplexing large numbers of spectral channels.

Time division multiplexing encompasses a broad range of high-bandwidth schemes. In TDM systems, data are transmitted serially, such that each bit corresponds to the optical intensity at an interval of time. One very important class of TDM systems are soliton systems, which use optical nonlinearities in fibers to overcome limits due to dispersion. Pulses are specially shaped so that dispersion and self-phase modulation effects cancel, thus allowing very long distance transmission. Pulse power stability is very important in soliton systems, and difficulties exist with generating and amplifying the pulses. In current systems, solitons are generated serially, and are still limited by the achievable serial electronic modulation bandwidth, though it is foreseeable that future TDM or WDM systems could also use soliton-shaped pulses to extend useful transmission distances.

TDM systems that use pulse shaping allow significantly increased bandwidths over single-channel systems. These systems involve duplicating the pulses from mode-locked laser sources, or reshaping one pulse into many. Pulse shapers are the most likely technology for ultrahigh bandwidth TDM systems, and are discussed in the next section. TDM systems that overcome the 10 GHz barrier will have significant problems with long-haul transmission, due to dispersion and nonlinear effects in fibers. One solution is to extend the function of the pulse shapers to shape the pulses into soliton configurations, such that dispersion and nonlinear effects cancel. Many of the recent WDM dispersion-reduction schemes mentioned above will also help extend the useful range of TDM systems.

The primary goal of this program was to demonstrate the feasibility of a channel with a continuous bandwidth on the order of one terahertz. This would greatly extend the current capability of communications systems, and may eventually be useful for ultrafast optical computing. Direct modulation of an optical source at terahertz speeds is impossible, so any system involving such a high bandwidth must rely on parallel approaches. One such approach is modulating several sources in parallel, as in the WDM systems discussed above. Another approach is modulating a single high-bandwidth source using parallel inputs in a complex modulator. This program focused on the latter approach through the use of pulse shaping. Pulse shaping has become a more viable technology in the recent past because of progress in high-bandwidth sources and amplifiers. Mode-locked solid-state lasers have advanced significantly, and mode-locked semiconductor sources and rare-earth-doped fiber lasers offer promise as effective sources for communications systems. Rare-earth-doped fiber amplifiers offer promise for pulse-shaping methods which may otherwise suffer from poor efficiency.

A pulse shaper is a broad term for devices that modulate broadband sources. Pulse shapers come in many forms. Important issues are size, resolution, time-bandwidth product (number of degrees of freedom or channels), reliability, and integrability. For useful ultrafast signal

6

generation, a pulse shaper must (1) encode data at the source bandwidth, on the order of 1 THz, (2) be reconfigurable on a time scale on the order of the packet length, must (3) interface well with optical fibers and integrated devices, and (4) be efficient and cost-effective enough for viable deployment. In this thesis, experiments with the distributed Bragg pulse shaper are presented which demonstrate that (1) is possible. As an integrated single waveguide device, the distributed Bragg pulse shaper is much more compact and robust than previously demonstrated pulse shapers and therefore satisfies (3) and (4) well. The ability of the DBPS to satisfy (2) is not demonstrated here, but is discussed in the context of currently available technologies.

One of the most popular forms of pulse shapers is the Fourier-plane pulse shaper [1], in which a grating and lens are used to disperse the component frequencies of a broadband optical source, and focus them in a Fourier plane. In this Fourier plane, a filter is used to modify the phase and/or amplitude of the frequency components. The beam is then recombined into a shaped temporal pulse using a complementary lens and grating. Various filtering technologies have been demonstrated, including fixed masks capable of modifying amplitude, phase, or both. Programmable filters have also been demonstrated, including liquid crystal phase modulators [2], simultaneous phase and amplitude modulators, Fourier-transform holograms, and acousto-optic filters [3]. Unfortunately, the programmable liquid crystal masks suffer from a finite resolution due to pixel size, and are not reconfigurable on the time-scales necessary for continuous terahertz operation. Acousto-optic filters are faster, but still orders of magnitude less than what is required. Some holographic methods in nonlinear materials have sufficiently fast response times, but these require high-power lasers and are unsuited for communications systems.

Many holographic pulse-shaping methods have been proposed and demonstrated. Holographic methods can be used to record and reconstruct arbitrary pulse shapes [4-7] but are unsuited for arbitrary pulse generation. Programmable volume holography has been demonstrated[8-10], including the ability to program arbitrary three-dimensional pulsed images [11]. These holographic pulse-shaping methods also demonstrated the importance of device geometry.

The reflection geometry has been chosen for the distributed Bragg pulse shaper because reflection geometries offer important advantages over transmission approaches. Holographic systems have the greatest spectral sensitivity in reflection geometry [12]. The sensitivity of reflection pulse shapers scales linearly with length, whereas the sensitivity of transmissive systems scales with device volume. The distributed Bragg pulse shaper has the advantage of spatially distributed modulation, and a simple space-to-time mapping between input channels and components of the output pulse. A static pulse-shaping system based on multiple reflections, similar to the distributed Bragg pulse shaper, has been demonstrated.

Other pulse shaping technologies exist which may be able to encode information at high speeds, including grating-coupled waveguides and acousto-optic tunable filters. These systems are only capable of very short pulse trains because they are transmissive, and do not make use of the volume of the device like reflective approaches.

This report considrs the distributed Bragg modulator as a coherence-domain encoding source for an ultrafast point-to-point communications system. We describe the theory, design and implementation of the pulse shaper under this program in some detail. Following our discussion

of the encoding side, we consider work under this program to develop receivers for DBPS signals using quantum dot and interferometric systems. In a sense, the receiver problem is less critical because systems capable of decoding ultrafast time, wavelength and coherence domain signals exist. Nevertheless, this program demonstrated that radically new approaches were possible and that these approaches could yield significant improvements in system performance and parallizability.

THEORY AND DESIGN OF THE DISTRIBUTED BRAGG PULSE SHAPER

The distributed Bragg pulse shaper is sketched in Figure 1. It consists of a series of Bragg reflector segments acting on light propagating in a waveguide. An optical pulse is launched into the waveguide and propagates along the device. The center frequency of this pulse is matched to the nominal resonance of the Bragg reflectors, so the pulse is reflected in a spatially distributed manner from each grating segment as it propagates along the waveguide. Contacts on each reflector induce an electric field and/or inject carriers locally along the grating. The change in refractive index in the vicinity of the grating section causes the Bragg resonance frequency of a modulated grating segment to shift. If the Bragg resonance of the segment is shifted sufficiently from the pulse center frequency, reflection will cease in that segment. Because a given region reflects light only in the time window corresponding to the pulse's presence in that region, turning the reflection off in a given region corresponds to turning off a specific window in the output pulse packet.

One may consider the distributed Bragg pulse shaper to be a series of partially reflecting mirrors. Each mirror may be turned on or off electrically. In device operation, the mirrors are set to a desired configuration of "on" and "off" states, and then a pulse is launched longitudinally through the mirrors. The pulse is partially reflected by "on" mirrors and is unaffected by "off" mirrors. As the pulse propagates through the device, it is reflected from the grating segments, producing an output packet which is the superimposed reflections from "on" mirrors. Each reflection is delayed by the transit time to each "on" mirror and back. Thus the serial shape of the reflected field corresponds to the spatial pattern of the mirror state. After the encoded wavepacket has left the device, the device is reconfigured for the next input pulse. The propagation time between mirrors determines the temporal separation of bits in the reflected signal. The total propagation time into the series of mirrors and back out determines the wavepacket length. In practice, multiple reflections and other second-order scattering effects may alter this picture, but such effects can be accounted for in filter design.
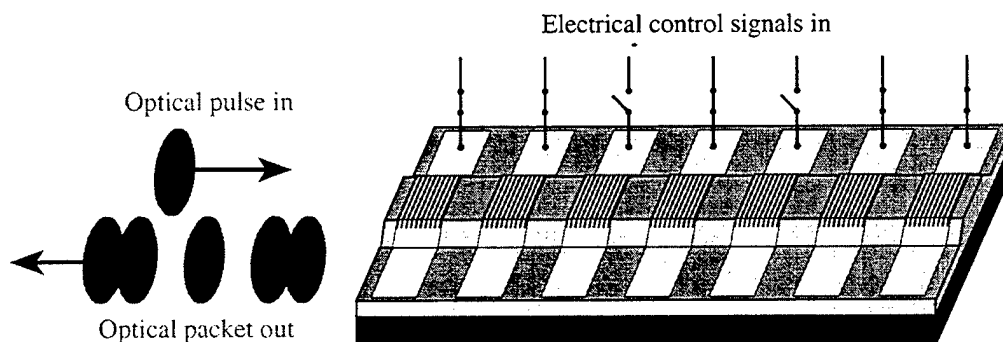
Electrical control signals in

Optical pulse in

Optical packet out

Figure 1 Distributed Bragg pulse shaper.

Device geometry is an important issue in pulse shaper design. The reflection geometry has been chosen because it offers two important advantages over transmission approaches. To understand the first advantage, it must be emphasized that wavepacket encoders can always be considered complex programmable filters. The spectral resolution of such filters depends on scattering geometry and device volume. The spectral resolution per unit device volume for reflection filters is orders of magnitude greater than for transmission approaches because spectral sensitivity of reflective scattering is greater and because the sensitivity of reflection approaches depends linearly on device length, while the sensitivity of transmission approaches is linear in device volume. The second advantage of reflection geometries is that they allow spatially distributed modulation. A spatially local modulator, like a shutter, requires a very large change in effective index or absorption to obtain high contrast. A section of distributed Bragg reflector can achieve very high contrast modulation using a change in effective index of less than one percent.   Although similar results can be obtained by modulating distributed transmission modulators or Fabry-Perot filters, these devices extract a substantial cost in modulator volume or sensitivity.

For maximum bit rate, the encoder is to be designed for continuous operation. For a 100-1000 bit packet length at 1 THz, the packet length will be 100 ps - 1 ns. Thus, the encoder will ideally operate at 1-10 GHz.   Such frequencies exclude thermal effects, acoustic effects, and electromechanical effects such as liquid crystal orientation or microelectromechanical modulation. Electro-optic effects are capable of such speeds, however. Electro-optic effects are available in a variety of materials, with semiconductor devices providing the largest available refractive index changes among integrated-optic-compatible materials.

The $Al_xGa_{1-x}As$ material system is well-suited to the distributed Bragg pulse shaper. This materials system was chosen because of convenient and well-developed fabrication processes, and the availability of facilities at the University of Illinois. $Al_xGa_{1-x}As$ has a continuously adjustable refractive index, is lattice matched for all values of the aluminum content x, and is capable of producing large index changes, as is typical of optical semiconductor materials. At the Center for Compound Semiconductor Microelectronics (CCSM), processes have already been developed and characterized for fabrication of gratings, waveguides, and electrical contacts. $Al_xGa_{1-x}As$ was chosen over other semiconductor systems because, for reasons of convenience, the devices will be tested with a Ti:sapphire laser, and this is tunable around the bandgap in this

material system. Ultimately, it will be desirable to move future devices to 1.3 μm or 1.55 μm, to be matched with rare-earth-doped fiber laser sources at communications wavelengths.

The Bragg pulse shaper is a ridge waveguide device, with sections of Bragg grating etched into the waveguide. A schematic of the device is shown in Figure 2. It is desirable to have good coupling between the free-space optical mode and the waveguide when lens coupling the Ti:sapphire laser into the waveguide. The epitaxially grown waveguide is thus designed to minimize coupling losses. Ideally, the waveguide would be as thick as the 1-2 μm spot sizes that are typically achievable from focused lasers. However, due to the high index (on the order of 3.5) of $Al_xGa_{1-x}As$, single-mode waveguides on the order of 1-2 μm require very slight refractive index (aluminum concentration) changes. In practice, the MOCVD reactors that are available for this project have finite tolerances for aluminum composition, so it is undesirable to require index changes that are too subtle. Also, small index changes for large single-mode waveguides lead to poor confinement. This is a complication because it is desirable to keep the mode confined within the low-doped waveguide core, to avoid excessive absorption due to the more heavily doped cladding layers. In addition, the evanescent tails of a poorly confined mode will interact more strongly with the substrate (GaAs, which is absorptive at the operating wavelength) and with the surface, which includes losses due to interactions with the metallization and surface roughness. Large waveguides require long growth times on the MOCVD reactor, adding expense. The waveguide design must thus be a compromise between these factors.
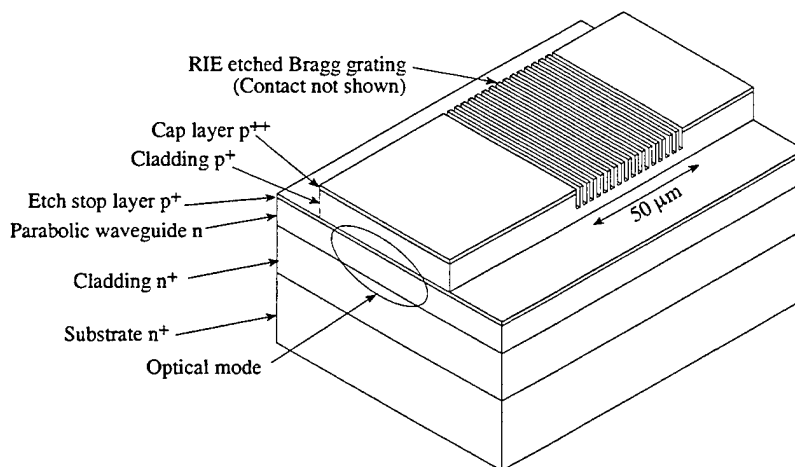

RIE etched Bragg grating
(Contact not shown)

Cap layer p++

Cladding p+

Etch stop layer p+

Parabolic waveguide n

Cladding n+

Substrate n+

Optical mode

50 μm

Figure 2 Structure of the distributed Bragg pulse shaper.

Of the simple waveguide designs available (square, linearly graded, parabolic), the parabolic waveguide is desirable because it offers large mode sizes and most effectively limits the spreading of evanescent mode tails away from the waveguide region. The distributed Bragg pulse shaper is thus designed as a parabolically index-graded $Al_xGa_{1-x}As$ structure eptiaxially grown on a GaAs substrate. A parabolic structure is also convenient from a crystal growth perspective, because in the MOCVD reactor, the column III reactant flows (trimethylgallium and trimethylaluminum) are varied linearly to achieve the parabolic grade in aluminum composition.

The waveguide is modeled via computer using a set of input parameters (such as aluminum concentration and waveguide height) to estimate the performance of the 2-D waveguide mode and the Bragg reflection gratings. The input parameters and then adjusted and

the program run iteratively to reach a compromise between the desired performance criteria. The criteria for the design are as follows:

- Single mode. The waveguide must have a single mode in both the epitaxial and lateral dimensions.
- Mode size. As discussed above, it is desirable to have large mode size to reduce losses incurred in lens coupling of the input laser.
- Low loss. The waveguide loss is strongly affected by the mode confinement in the epitaxial direction. The evanescent tail of the mode will interact with the substrate and surface, causing losses. The GaAs substrate is highly absorbing at the operation wavelength, so a significant buffer layer is needed between the substrate and waveguide. The surface is also a source of loss, due to roughness from the grating etch and waveguide etch, and the presence of metallization. Doping is also a factor in loss, as dopants increase absorption. The p-i-n device is designed with low doping in the waveguide core to reduce this absorption.
- Appropriate Bragg grating strength. Useful pulse shapers will employ large numbers of weak gratings. However, for demonstration purposes, the devices in this thesis are designed to have high (on the order or 1-10%) diffraction efficiencies per grating section. In general strong reflections require strong interactions with the surface-etched grating, which involves trade-offs with waveguide loss, mentioned above.
- Good lateral confinement. Increasing lateral confinement will decrease the overlap of the mode with the rough edges of the waveguide, thus decreasing scattering losses. The degree of lateral confinement also affects the acceptance angle of the waveguide. Confinement must be sufficient to achieve reasonable acceptance angles for coupling into the waveguide.
- Reasonable fabrication. The device must be reasonable to fabricate using the facilities that are available. This includes realistic times for crystal growth and etch processes, as well as reasonable tolerances. The design must be tolerant enough that expected variations in growth, doping, and etch processes still yield usable devices.

The waveguide modes are modeled using a Matlab program developed by the author. The program uses numerical integration of the 1-D TE wave equation to solve for the effective index of the slab mode in the waveguide region. This mode is solved for both as-grown waveguide and for the etched lateral cladding regions. To find the 2-D confined ridge modes the effective index approximation is used, in which the lateral mode is approximated as a 1-D TM mode with a core index equal to the as-grown mode effective index and a cladding index equal to the etched-region effective index. This TM mode is then solved and confinement factors and mode sizes are calculated to estimate the performance of the waveguide device.

The computer program starts with user-supplied input values including the wavelength, information about the epitaxial layers including layer thickness, aluminum composition, and doping, and information about the processing including waveguide width, etch depth and grating etch depth.

The 1-D TE wave equation is given by

$$\left(\frac{\partial^2}{\partial x^2} + \frac{\partial^2}{\partial z^2} + \omega^2 \mu \varepsilon(x) \right) E_y = 0 . \tag{2.1}$$

The solution $E_y = \hat{y}E(x)e^{ik_z z}$ is inserted into this equation to give the eigenvalue equation

$$\frac{\partial^2}{\partial x^2}E_y + \left(\omega^2 \mu \varepsilon(x) - k_z^2\right)E_y = 0. \tag{2.2}$$

This equation can be discretized on a mesh of N points to give the difference equation

$$\frac{E_{n+1} - 2E_n + E_{n-1}}{\Delta^2} + \left(\omega^2 \mu \varepsilon_n - k_z^2\right)E_n = 0. \tag{2.3}$$

ε_n is given values to represent the relative permittivity of the waveguide on the range of values $x_n = n\Delta$, with separation Δ between points. The permittivity is calculated to include the effects of aluminum concentration and doping, based on published data. The values of x start with x_0 and x_1 representing the air above the waveguide and range to x_N in the lower cladding. Given an initial guess for the eigenvalue k_z, and two initial values E_0 and E_1, this difference equation can be solved for the mode profile E_n. A guided mode will be evanescent in the air above the waveguide, so the initial values are related by $E_1 = E_0 e^{\alpha \Delta}$, where the decay constant is given by $\alpha = \sqrt{k_z^2 - \omega^2 \mu \varepsilon_0}$. E_0 can be assigned the arbitrary initial value of 0.0001, as the mode profile is normalized after the calculation.

The initial guess for the eigenvalue k_z is provided by solving the wave equation using a matrix method for a small number of points N. The difference equation, (2.3), can be written as

$$\Delta^2 k_z^2 E_n = E_{n+1} - (2 - \Delta^2 \omega^2 \mu \varepsilon_n)E_n + E_{n-1}, \tag{2.4}$$

or

$$\lambda E_n = E_{n+1} - f_n E_n + E_{n-1} \tag{2.5}$$

where $\lambda = \Delta^2 k_z^2$ and $f_n = 2 - \Delta^2 \omega^2 \mu \varepsilon_n$ have been defined. The difference equation can then be written as the matrix eigenvalue equation $\lambda \overline{E} = \overline{\overline{M}}\,\overline{E} + \overline{C}$, where

$$\overline{\overline{M}} = \begin{bmatrix} f_1 & 1 & & & 0 \\ 1 & f_1 & 1 & & \\ & 1 & f_1 & 1 & \\ & & 1 & \ddots & \ddots \\ 0 & & & \ddots \end{bmatrix}, \tag{2.6}$$

and $\overline{C}$ determines the boundary conditions. A quick approximate solution to this equation can is obtained by forming an initial guess for the vector $\overline{E}$, which is a half sine wave (the approximate shape of the first mode) with maximum amplitude 1. This vector is multiplied by the matrix $\overline{\overline{M}}$, and boundary conditions are imposed by forcing the endpoints to represent evanescent waves in the air ($\varepsilon = \varepsilon_0$), and in the lower cladding ($\varepsilon = \varepsilon_3$), such that

$$E_1 = E_2 \exp(-\sqrt{\Delta^2 k_z^2 - \Delta^2 \omega^2 \mu \varepsilon_0})$$
$$E_N = E_{N-1} \exp(-\sqrt{\Delta^2 k_z^2 - \Delta^2 \omega^2 \mu \varepsilon_3})$$

(2.7)

This result is normalized to maximum amplitude 1. The normalized eigenvector is plugged back into the matrix eigenvalue equation as the next guess, and the normalization constant is used as the eigenvalue. After 20 iterations, a sufficiently accurate guess for the eigenvalue is obtained.

This eigenvalue is then used as an initial guess, and (2.3) is solved for the mode profile E_n on a finer discretization mesh, starting in the air and solving the difference equation to the lower cladding. This equation is then solved iteratively, adjusting the eigenvalue k_z until the mode is properly evanescent in the lower cladding. This gives a good solution to the 1-D wave equation in the parabolic waveguide region.

This effective index calculation is repeated four times, for the as-grown (unetched) material, for the material in the lateral cladding regions after the waveguide etch, and for these waveguide and cladding regions etched to the depth of the designed Bragg grating etch. The 2-D mode is calculated using the effective index approximation, first using the unetched waveguide and etched cladding layers to compute the effective index of the 2-D mode without the Bragg grating. Then the calculation is repeated for the same waveguide etched to the Bragg grating depth. The difference between these two effective indices gives the amplitude of the refractive index modulation $2\Delta n$ caused by the Bragg grating. The gratings are third order, so the calculated index modulation Δn is multiplied by $4/3\pi$, the amplitude of the third Fourier component of the (50% duty cycle) square grating corrugation, to estimate the amplitude of the index modulation at the optical wavelength. The diffraction efficiency of the sections of gratings is calculated, and plotted as a function of the length of the grating.

At completion of these calculations, the program plots the vertical and lateral 1-D mode profiles, displays the calculated effective indices, confinement factors, and acceptance angles, and gives the free space grating period that should be written for the third-order grating. These results are examined and the program run repeatedly until an appropriate set of design parameters are found.

The reflectors in the distributed Bragg pulse shaper are sections of third-order Bragg grating etched into the waveguide. The gratings are created by a direct electron-beam write in PMMA resist, and transferred into the device using Reactive Ion Etching (RIE). Because of the resolution of those processes, it is only practical to make features on the order of 150 nm or larger. For this reason, the distributed Bragg pulse shaper is made with third order Bragg gratings, with periods on the order of 350 nm.

Several effects must be considered when designing gratings for the distributed Bragg pulse shaper. It is known that the correspondence between spatial grating shape and temporal pulse shape in reflective pulse shapers breaks down when the total device diffraction efficiency exceeds 50%. In general, higher diffraction efficiencies lead to depletion of the source pulse and multiple reflections that distort the output packet. Pulse shapers of total diffraction efficiency on the order of 25% or less yield acceptable solutions to these problems. The pulse

shapers presented in this thesis were designed with grating reflectivities on the order of 1% to 10%, to facilitate easier detection of diffracted pulses. Practical pulse shapers will have a larger number of grating sections, and thus smaller diffraction efficiencies per section.

Switching in the distributed Bragg pulse shaper is attained by modulating the net refractive index in the region of a grating section, thus shifting the reflection spectrum of that grating segment off-resonance with the wavelength of the input pulse. This is illustrated below for the case of the second- and third-generation distributed Bragg pulse shapers.

A section of Bragg grating 50 μm in length has a reflection spectrum with a full width at half-max (FWHM) of 2 nm, which corresponds to a 300 fs optical pulse. This is illustrated in Figure 3. Figure 3(a) shows the reflection spectrum of a 50 μm section of grating (this model assumes a lossless grating with no refractive index dispersion), and the spectrum of a 300 fs pulse at a center wavelength of 815 nm. The overlap is maximized, so the reflectivity is maximized. Figure 3(b) shows the same spectra, after the average index in the grating region has been changed by $\Delta n = 0.016$. Since the spectra no longer overlap well, little of the input pulse will be reflected, and the grating reflection has essentially been changed from an "on" to an "off" state. Note that it is also possible to design a device which is normally in the "off" state, and uses index change to shift the Bragg grating into resonance with the input pulse.
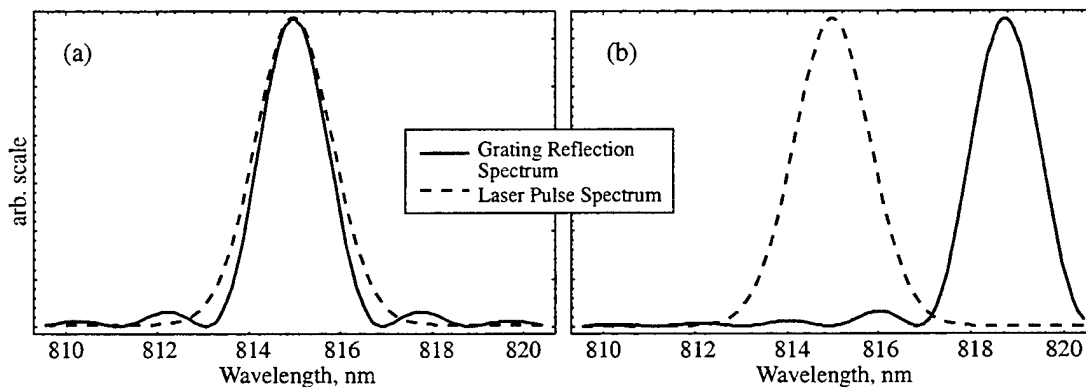
Figure 3   Input   pulse   spectrum   and   grating   reflection   spectrum. (a) Unmodulated grating (b) Grating after index change $\Delta n = 0.016$.

The gratings sections start and end abruptly, giving a square impulse response, and thus a $\sin(x)/x$ reflection spectrum. The oscillations outside the central lobe of this reflection spectrum cause unwanted reflections in the "off" state. This effect could be removed, by apodizing each grating segment such that the temporal impulse response was Gaussian in nature, thus giving a Gaussian reflection spectrum. Other filter designs, such as $\sinh^2$ or square reflection spectra are also possible.

FABRICATION AND TESTING OF THE DISTRIBUTED BRAGG PULSE SHAPER

Pulse shapers fabricated under this program can be divided into three generations. The first generation of pulse shapers were simply gratings on waveguides, without doping or

electrical contacts necessary for electrically-induced modulation. The second-generation pulse shapers were doped to form a pn junction and electrically contacted. The third-generation pulse shapers came after major changes in the fabrication procedure, and had continuous gratings along the waveguides to avoid unwanted reflections from discontinuities. Several iterations of design, fabrication, and testing were performed to make these pulse shapers, so it is necessary to explain nomenclature so that the devices can be referred to accurately. This section will briefly introduce the naming of the devices and the major features of each round of devices. The first step in device design is the computer modeled design for epitaxial growth. Devices are numbered according to this crystal growth. Usually the sample that is grown is large, and is thereafter cleaved into a number of samples, each given another number to identify it. As subsequent pieces are cleaved off these pieces for waveguide etches or electron-beam writes, they are given another number. For example, sample 14.1T1 H1 is a device from the 14th epitaxial design, the first piece broken off, the first electron-beam write on that piece, eventually cleaved into a bar labeled H1. Table 1 lists the epitaxial layer designs, and information about the features of the devices made with that material. The earlier devices were fabricated by Gary Smith, S. David Roh and Ken Purchase. The MOCVD crystal growth for all devices was performed by Mark Osowski and S. David Roh.

Epitaxial Growth Design	Fabricated by	Comments
Waveguide 1 - Waveguide 6	N/A	Initial designs made in a variety of sizes
Waveguide 7	Gary Smith	Slab waveguide with no lateral confinement, and large-area Bragg gratings. Did not yield significant data
Waveguide 8	N/A	An alternate design to Waveguide 9. Never fabricated.
Waveguide 9	Gary Smith	The first First-Generation device. Demonstrated THz pulse train. No electrical contacts.
Waveguide 10	N/A	An alternate design to Waveguide 11. Never fabricated.
Waveguide 11	Gary Smith, Ken Purchase, and S. David Roh	The first Second-Generation device. Included doping and electrical contacts. Gratings were damaged in etch. Only produced index change data.
Waveguide 12a	Ken Purchase	Discovered problems with citric acid etch.
Waveguide 12b	Ken Purchase	A second growth run of the same design. Gratings written after the waveguide etch. Gratings were etched too deep, and led to anti-guiding in the waveguide. Did not yield significant data.
Waveguide 13.2	Ken Purchase	Reflection from discontinuities at edges of grating larger than grating reflection. Did not yield significant data.
Waveguide 13.1	Ken Purchase	The first Third-Generation Pulse shaper. Used continuous gratings along waveguide. Sample was too small to apply electrical contacts.
Waveguide 14	Ken Purchase	A new mask for narrower waveguides. Smaller waveguide dimensions. Demonstrated switchable reflections.

Table 1 Implementations of the distributed Bragg pulse shaper.

It is important to note that any of these names, such as Waveguide 14, refers to a whole family of devices made using one initial design and one semiconductor growth run. However during processing, devices are often cleaved into smaller pieces (often as many as 30) to test etches, to allow easier electron-beam alignment, or to offer a range of etch depths or electron-

beam doses. Only a small number of the pieces survive all the processing to become completed devices. In the following sections, the three major generations of pulse shapers are described.

First Generation Pulse Shaper

The first-generation distributed Bragg pulse shaper, Waveguide 9, is depicted in Figure 4. The waveguide consists of a 1.3 μm waveguide layer, with a symmetric parabolically-graded aluminum composition ranging from 20% at the center to 23% at the outer edges. This change from 20% to 23% was chosen because it was the minimum difference that was expected to be reliably grown by the MOCVD hardware. The 1.3 μm waveguide thickness was chosen as a compromise between the need to have a thick waveguide and the desire not to have the mode extend too far towards the substrate. The lower cladding (also serving as a buffer layer) is 1 μm thick, and the upper cladding is 0.4 μm thick. Both are $Al_xGa_{1-x}As$ with 23% Al. Although the optical mode is well confined within the parabolically graded section, the AlGaAs cladding regions are still necessary to avoid high absorption of mode tails by the GaAs substrate, and excessive interaction with the surface. The whole structure is undoped. In the center of the parabolically-graded waveguide is a 100 Å etch-stop layer made of $Al_{0.6}Ga_{0.4}As$. On top is a 0.1 μm GaAs cap layer, to prevent formation of native aluminum oxides on the surface in contact with air.

The waveguides are designed to be 5 μm wide, etched to a depth of 1.045 μm (down to the etch-stop layer). The Bragg gratings are designed to have 1.5% diffraction efficiency per grating section at the center wavelength. The grating sections are 17.3 μm long, and repeat at a period of 34.6 μm. This gives a designed etch depth for each Bragg grating section of 0.4 μm. As mentioned previously, the gratings are third-order gratings with a 50% duty cycle. The computer model predicts an effective index in the grating sections of 3.518, which gives a grating period of 347.5 nm for light at 815 nm.
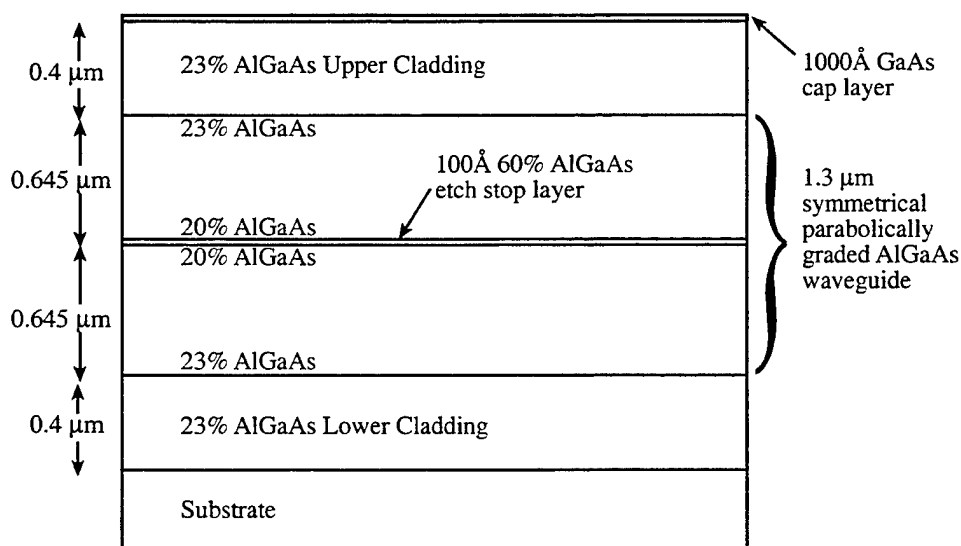

Figure 4. Epitaxial layer structure for Waveguide 9.

The Bragg pulse shaper was fabricated using techniques previously developed for DBR and DFB lasers, although some modifications have been made due to differences in the character of these devices. The waveguide structure was grown on an n-type GaAs wafer by atmospheric pressure metalorganic chemical vapor deposition (MOCVD). A 600 Å layer of silicon dioxide was then grown by plasma-enhanced chemical vapor deposition (PECVD). The sections of Bragg grating were exposed in PMMA resist using a direct electron-beam write. The grating was made 50 µm wide, to simplify alignment of the 6 µm waveguide over the gratings. The developed PMMA pattern was etched using two steps of reactive ion etching (RIE). In the first step, the grating pattern is transferred from the PMMA into the silicon dioxide using Freon-23, and then in the second step the pattern is transferred into the $Al_xGa_{1-x}As$ layers using $SiCl_4$.

After the grating etch, the remaining oxide was removed (again using Freon-23 RIE), and a new 800 Å oxide layer was grown via PECVD. A 6 µm wide waveguide pattern was defined in photoresist, etched into the oxide, and then wet-etched into the $Al_xGa_{1-x}As$ using a citric acid-hydrogen peroxide solution. This is an isotropic etch, which is intended to stop at the $Al_{0.6}Ga_{0.4}As$ etch-stop layer. Undercutting caused the resulting waveguide to be about 5 µm wide. The samples were thinned to 125 µm and cleaved into bars. Bars were examined in a microscope, and the best samples were selected for antireflection coating. The coating reduces the reflection of the facet from approximately 30% to 6%. The devices were mounted on the end of thin aluminum stock for testing.

Figure 5 shows a close-up view of the waveguide, and Figure 6 shows a view of the whole device. Note that the waveguides are fabricated at an angle (approximately 5•) with respect to the cleaved facet. This is to allow separation of the signal packet from input facet reflections during testing.
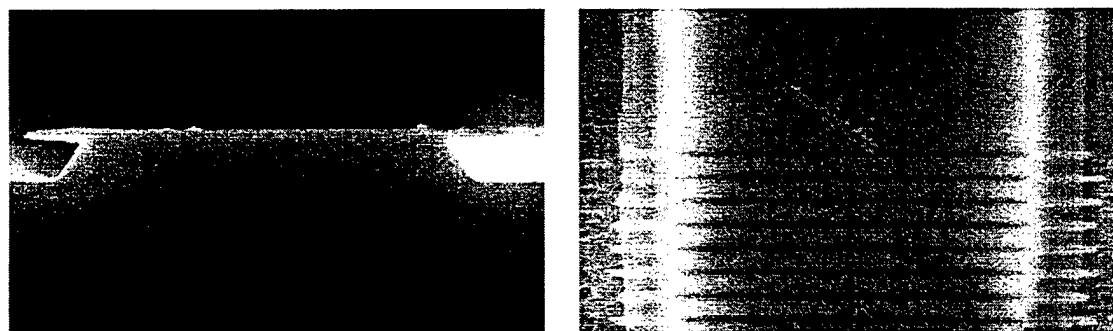

Figure 5 Distributed Bragg pulse shaper. Left: Entrance facet of waveguide. Right: Top view of waveguide and a section of Bragg grating. In both images the SiO₂ etch mask hangs over the etched waveguide.
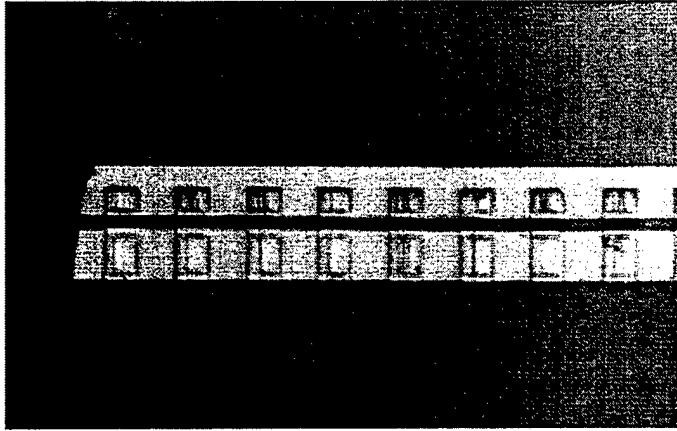
Figure 6 Distributed Bragg pulse shaper. The dark line in the middle is the waveguide, perforated by sections of Bragg grating. The left edge is the angled cleaved entrance facet.

Optical Testing

The pulse shaper was tested using the setup in Figure 7(a). A 100 fs Ti:sapphire laser pulse at λ=800 nm is focused into the cleaved facet of the waveguide. The pulse propagates down the waveguide, and is reflected by sections of Bragg grating. The output of the device is the superposition of reflections of the input pulse. This output packet is detected in an interferometric cross-correlator, in which the output packet is combined with a reference pulse after a variable delay from a mirror on a motorized stage. The reference pulse and signal packet interfere on a CCD camera, and the video is digitized by a computer. The computer uses an FFT narrowpass filter to measure the amplitude of the signal at the expected fringe frequency. The computer then records the measured fringe intensity as a function of motor position.

The distributed Bragg pulse shaper that is used for this proof-of-principle research is designed for end-coupling with a lens. A major problem with this technique is that reflections from the front facet are large in comparison to the light that is coupled into the waveguide and reflects from grating sections. For testing purposes, it is necessary to reduce these reflections, as depicted in Figure 7(b). The laser is used off-center in the lens, and the resulting reflection of the input beam is strongly reduced by a beam block upon its return to the lens. The light that is coupled into the waveguide mode is radiated more symmetrically, and is only partially blocked by the beam block. This technique significantly reduces the intensity of the unwanted front facet reflection.
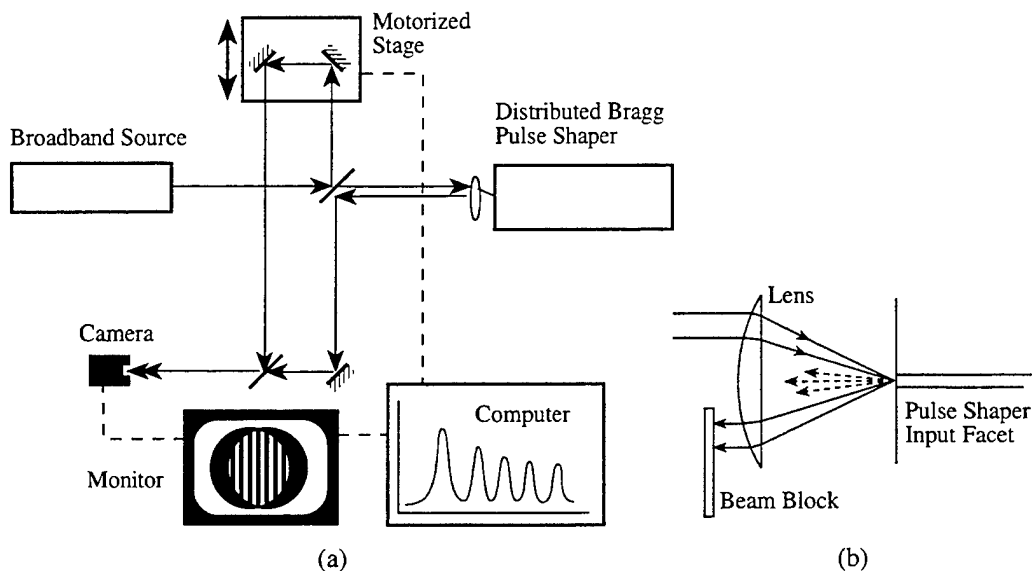
18

Figure 7 (a) Interferometric cross-correlation setup for testing the distributed Bragg modulator. (b) Beam block for reducing front facet reflection.

Figure 8 shows the terahertz pulse packet encoded by the device of Figure 6. Because the device was not doped and did not have electrical contacts, pulses in the output packet could not be modulated. Evident in the figure is a decay of the pulse train due to the losses from the weakly confined waveguide. Because the grating is third order, light is also lost through two orders of light diffracted toward the substrate of the device. Also evident in the figure is an apparent splitting or widening of pulses toward the end of the packet. It is believed that this splitting is because the waveguide is not single-moded.
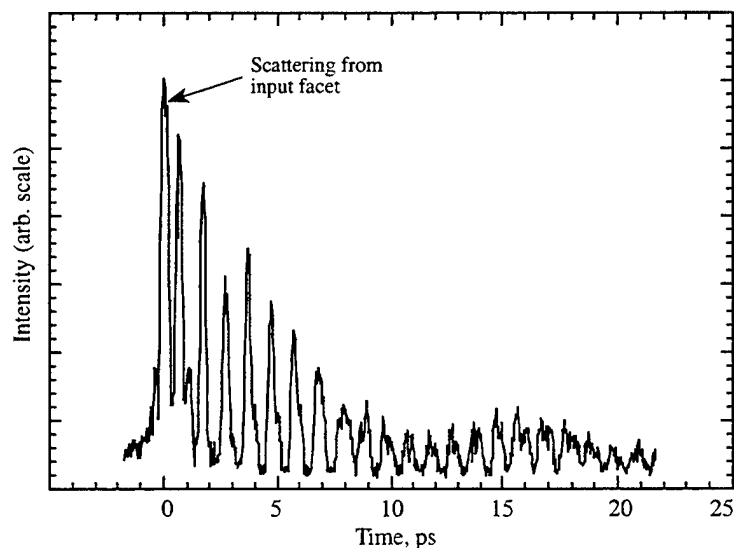
Figure 8 Terahertz output packet from the distributed Bragg modulator.

Second Generation Pulse Shaper

The second-generation design represented many changes from the previous waveguides. Most notably, the second-generation devices were to include electrical contacts, so doping the device to form a pn junction was necessary. The computer model up to this time had not included the effect of doping on the refractive index, and had only included an estimate for the refractive index as a function of percent aluminum composition. Then next device grown was Waveguide 11. The structure for this device is shown in Figure 9. The dimensions of the waveguide were substantially reduced to insure single-mode operation. The newer design also allows the mode to interact a little more strongly with the surface, to increase the strength of the Bragg grating.

Waveguide 11 consists of a 0.5 μm waveguide layer, with a symmetric parabolically-graded aluminum composition ranging from 17% at the center to 30% at the outer edges. The increased compositional range was necessary to achieve good confinement in the reduced size waveguide core. The core has a low n doping ($\bullet$ 10^{17} cm^{-3}), to reduce absorption associated with doping. The lower cladding (also serving as a buffer layer) is 1 μm thick, doped 2×10^{18} cm^{-3} n type, and the upper cladding is 0.5 μm thick, doped 2×10^{18} cm^{-3} p type. Both are Al$_x$Ga$_{1-x}$As with 30% Al. A 100 Å etch-stop layer made of Al$_{0.6}$Ga$_{0.4}$As is included 0.37 μm below the surface, and is also doped 2×10^{18} cm^{-3} p type. On top is a 0.1 μm GaAs cap layer, to prevent formation of native aluminum oxides on the surface in contact with air, and to provide good electrical contact. The cap layer is doped 1×10^{19} cm^{-3} p type.
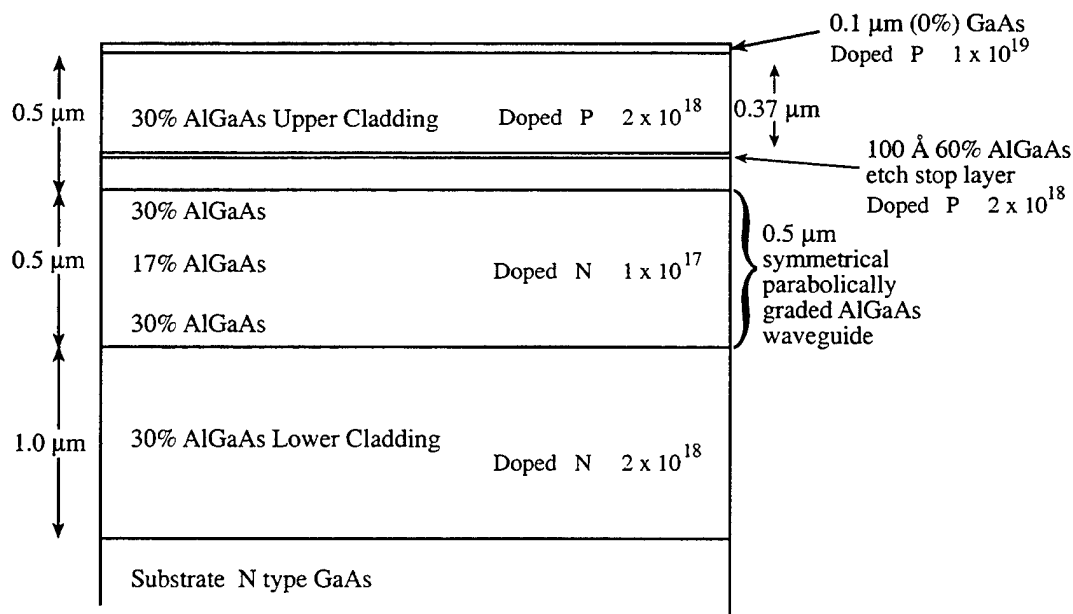

Figure 9. Epitaxial layer structure for Waveguide 11.

The waveguides were designed to be 4 μm wide, etched to a depth 0.37 μm. A new lithography mask was created to achieve this waveguide width and to provide the electrical contact pattern. The grating sections are 50 μm long, and repeated at a period of 100 μm. This larger grating size was chosen to allow enough room for contacts, such that contact pads were large enough for convenient wire bonding. The longer gratings also have a narrower reflection bandwidth, allowing the use of narrower bandwidth pulses. Conveniently, the combination of narrower grating reflection bandwidth and narrower pulse bandwidth requires less refractive index modulation to achieve switching. The Bragg gratings are designed to have 1.5% diffraction efficiency per grating section at the center wavelength. This gives a designed etch depth for each Bragg grating section of 0.35 μm. The computer model gives an effective index in the grating sections of 3.497, which gives a grating period of 349.6 nm for light at 815 nm.

The fabrication of Waveguide 11 was performed using the same techniques as for Waveguide 9, but also included the application of electrical contacts. After the waveguide was etched, the remaining oxide was removed, and a 1200 Å layer of silicon dioxide was applied for electrical insulation. A 3.5 μm stripe was etched using Freon-23 RIE in the oxide in the regions on top of the waveguide to allow electrical contacts. The p-type contact of 50 Å Ti, 50 Å Pt, and 1500 Å Au was deposited using image-reversal photoresist, evaporation, and liftoff. The samples were then thinned to 125 μm and n-type metallization consisting of 250 Å Ge and 1350 Å Au was evaporated on the back. The metals were alloyed by heating the sample in a hydrogen atmosphere over a period of 3 min to 390• C, waiting 10 seconds, and cooling. The samples were then cleaved into bars, sorted, and antireflection-coated as before.

After completing Waveguide 11, it was found that the gratings were damaged during the waveguide etch. The citric acid/ hydrogen peroxide etch is stable in bulk semiconductor, but is hard to control in the Bragg grating regions. Because of undercutting, and an insufficiently thick oxide mask in Waveguide 11, the Bragg grating was damaged to the point where no reflection from the grating was observable. Figure 10 shows the damaged grating of one of the Waveguide 11 samples.
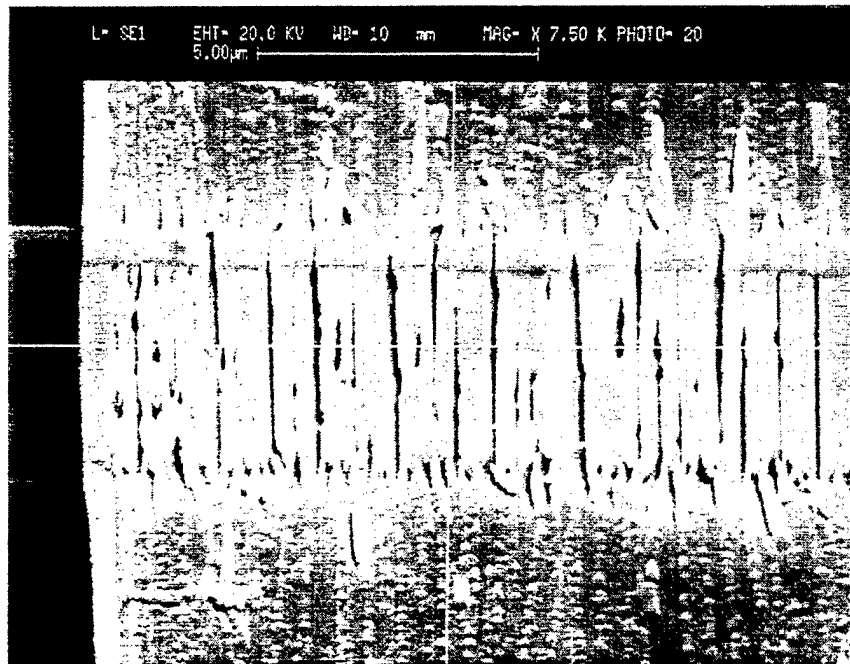
Figure 10. Grating damaged by citric acid/ hydrogen peroxide etch.

A picture of Waveguide 11 appears in Figure 11. The device is mounted on a high-speed mount as shown in Figure 12. The mount couples an SMA cable with a microstrip waveguide, and a matching resistor to efficiently deliver current to the device at high modulation rates. The mount is intended to deliver current to one contact of the distributed Bragg pulse shaper.
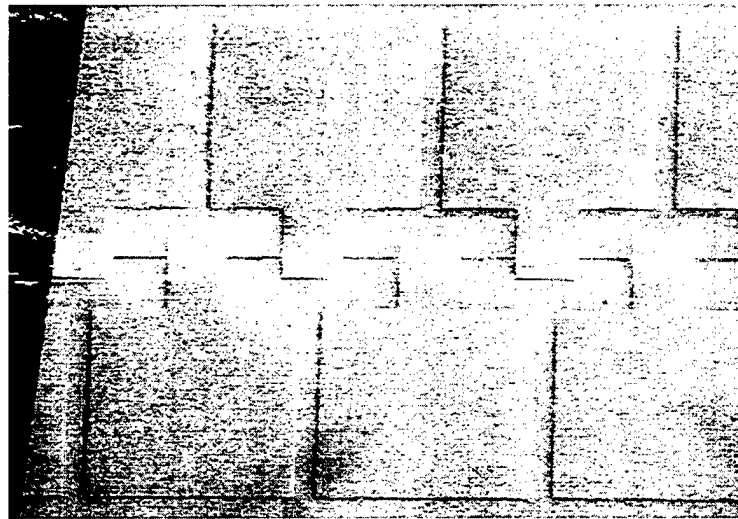

Figure 11 Distributed Bragg pulse shaper. The thin line is the waveguide, with large gold contacts covering the 50 μm grating sections of the waveguide.
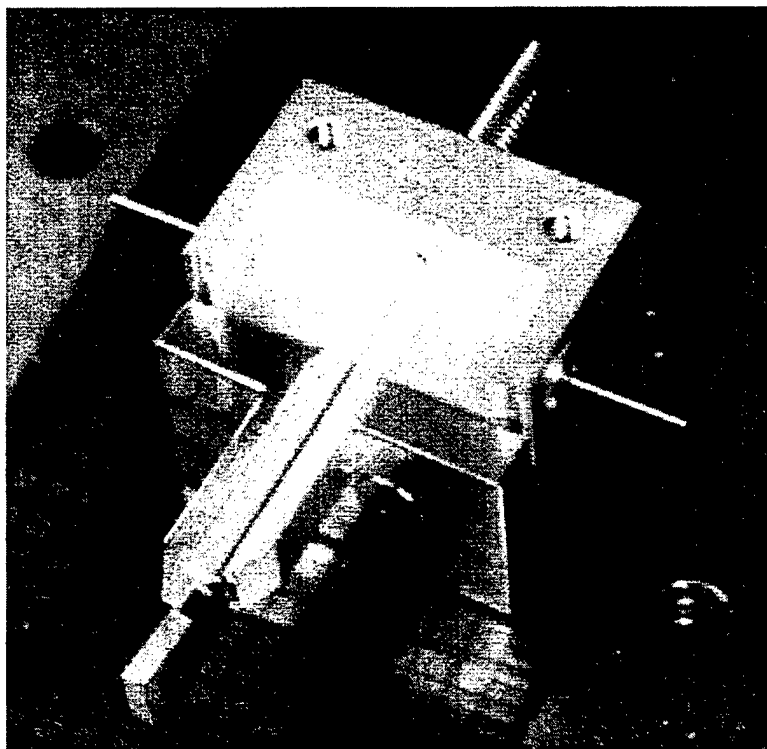
Figure 12. Distributed Bragg pulse shaper in high-speed electrical mount.

The temporal waveform reflected from the damaged Waveguide 11 samples was measured. This waveform is shown in Figure 13. The figure clearly illustrates that reflections from the gratings are not visible, but strong reflections are evident from point defects in the waveguide. It was possible to use these defects to advantage in making a measurement of the index change produced in these devices. The motor was positioned to produce interference between the reference pulse and a strong reflection from a defect in the waveguide after the electrically contacted section. A dc current was applied to the device, and the phase shift of the interference fringes was measured as a function of current. The measured phase shift is shown in Figure 14. The extent of current spreading from under the contact is uncertain, but assumed small because of the highly localized distribution of current-induced spontaneous emission near the contact. Assuming current spreading from the electrode is negligible, the maximum index change observed was $\Delta n = 0.021$ at a current density of 16 kA cm^{-2}. This demonstration shows that the index changes necessary for demonstration of modulation in this material system are attainable, although the nature of the refractive index change mechanism is not characterized.
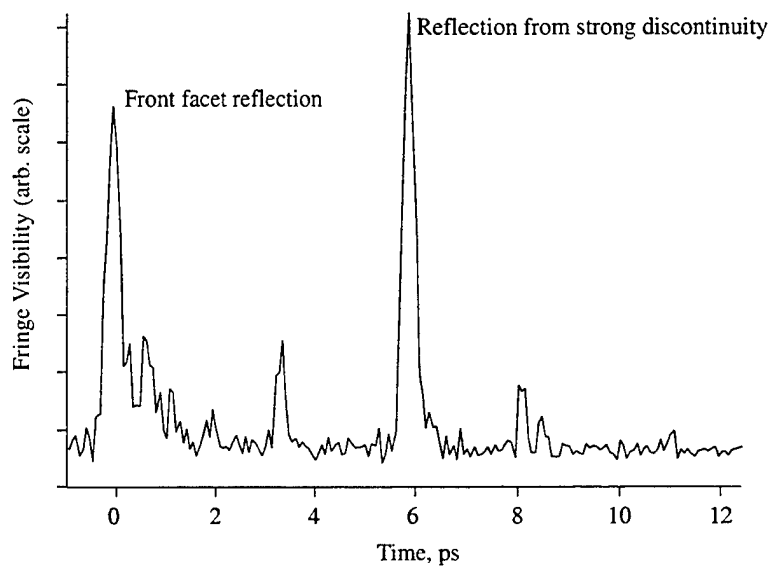
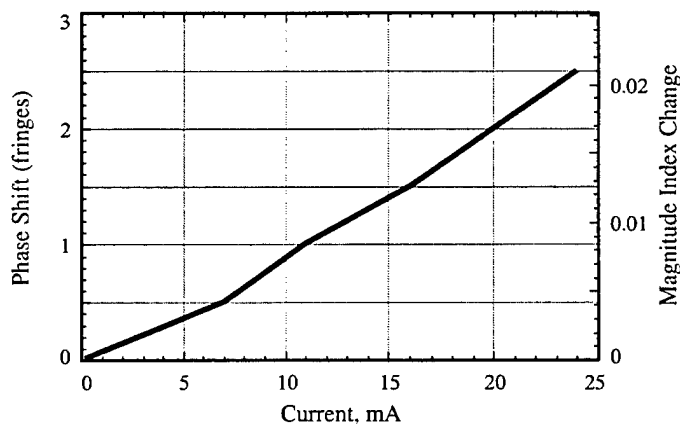**Figure 13 Temporal waveform from Waveguide 11.**

Figure 14 Measured Phase shift versus input current.

The gratings on Waveguide 11 were damaged by wet etching waveguides after the gratings were already etched into the epitaxial layers of the sample. The gratings were damaged because of an insufficiently thick oxide mask used during the waveguide etch process. However, this technique also has other disadvantages. This isotropic wet etch that is used to create the waveguides causes undercutting, in which the etched waveguide is narrower than the silicon dioxide mask. This in itself is not a problem, but areas of the sample in which Bragg gratings exist are etched at a faster rate than areas without gratings. In those regions where the waveguide is etched over sections of Bragg grating, the undercutting is more severe, yielding a slightly narrower waveguide. This same effect also caused the waveguide cladding etch to be deeper in regions where Bragg gratings exists. These two sources of discontinuity between the grating and nongrating regions of the waveguide lead to mode mismatches and discontinuities in the effective index of the waveguide, causing unwanted wavelength-insensitive reflections. Such reflections can not be turned off by modulation of the refractive index.

24

Third Generation Pulse Shaper

The issue of reflections from discontinuities and other fabrication difficulties were examined in the designs for Waveguides 12a, 12b, 13.2, and 13.1. Because none of these devices produced significant results, they will not be discussed in detail, but the principles learned in their fabrication were essential in the success of Waveguide 14. Details of the design and testing of Waveguide 14 are presented in this section.

In the design of Waveguide 14, it was desired to increase the reflectivity of the sections of Bragg grating to the order of 10%, so that reflections from sections of grating would be more readily visible. To achieve this, the width of the upper cladding was reduced, such that the Bragg grating could be etched closer to the center of the waveguide mode, to increase the interaction between the mode and the grating structure. The structure of Waveguide 14 is depicted in Figure 15. It is similar to Waveguide 11, but contains a thicker (5.3 μm) waveguide core region. The thickness of the upper cladding region has been reduced to 0.35 μm, and the cap layer reduced to 500 Å. Also the range aluminum composition in the parabolically-graded waveguide has been reduced, varying from 20% aluminum at the center to 30% at the edges. This reduction allows a larger mode, which will have more overlap and interact more strongly with the grating above. To prevent substrate absorption from this increased-sized mode, the lower cladding layer is increased to 1.5 μm thickness. The etch-stop layer was not included in Waveguide 14 because a new etch was used, as described in the next section. The waveguide was etched to a depth of 278 nm, and the Bragg grating was etched to a depth of 210 nm.
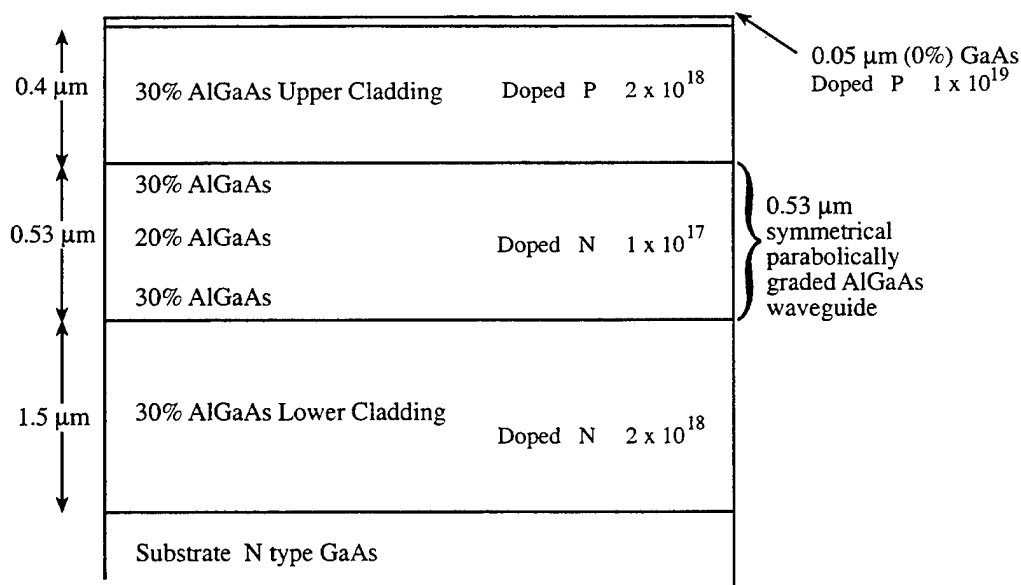
0.4 μm	30% AlGaAs Upper Cladding	Doped P	2×10^{18}	0.05 μm (0%) GaAs Doped P 1×10^{19}
0.53 μm	30% AlGaAs			0.53 μm symmetrical parabolically graded AlGaAs waveguide
	20% AlGaAs	Doped N	1×10^{17}	
	30% AlGaAs			
1.5 μm	30% AlGaAs Lower Cladding	Doped N	2×10^{18}	
	Substrate N type GaAs			

Figure 15. Epitaxial layer structure for Waveguide 14.

The design of Waveguide 14 representes a major change that addressed the problems of unwanted reflections arising from discontinuities between sections of the waveguide with reflectors and sections without. Any change from etched to unetched regions along a waveguide with periodically etched gratings causes a discontinuity in the effective index of the mode. To

resolve this problem, gratings are etched continuously along the entire waveguide, with a pitch that varies every 50 μm as shown in Figure 16. Alternate sections are designed to reflect at 806 nm and 783 nm (grating periods of 346 nm and 333 nm respectively), such that a laser pulse at 783 nm reflects only from the alternating sections with 333 nm period. Because there are no unetched sections of waveguide between the active reflecting sections, there is no discontinuity in the effective index of the mode at the start and end of the reflectors. This eliminates the unwanted reflections due to the previous discontinuities. Figure 17 shows a section of a Waveguide 14 made in this manner.
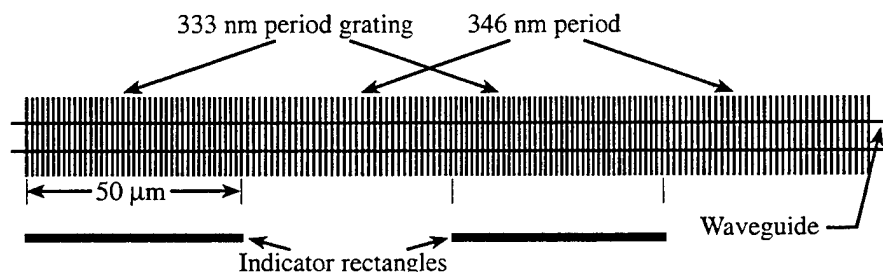
Figure 16. Alternating grating periods. Grating sections are printed four at a time within each ebeam field, and successive fields are stitched together to form a continuous grating. The indicator rectangles serve as a visual reference for aligning contacts.
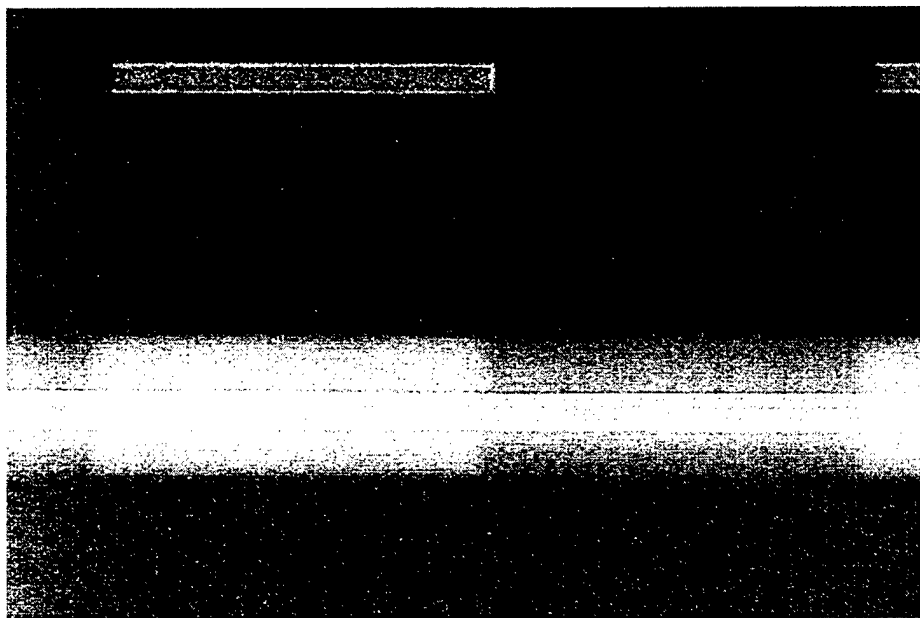
Figure 17. Scanning electron micrograph of the alternating gratings described above. The different grating periods show up as different shades due to Moiré interference with the beam in the scanning electron microscope.

After Waveguide 11, there were many changes to the fabrication procedure. Most notably, the gratings were etched after the waveguides, alleviating the problems with the waveguide wet etch damaging pre-etched gratings.

The epitaxial layers of Waveguide 14 were grown by MOCVD. Waveguides were then defined on an silicon dioxide mask, and etched in a solution of 1:8:80 H_2SO_4:H_2O_2:H_2O. This solution etches $Al_xGa_{1-x}As$ isotropically, and independently of aluminum content. This etch was used because it is reliable and repeatable, and the previously used citric acid-hydrogen peroxide etch frequently was not. An electron micrograph of an etched waveguide is shown in Figure 18. After etching, the mask was removed and 600 Å of silicon dioxide were deposited. Then photolithography, evaporation, and liftoff were used to create 4 µm gold squares on the sample for alignment during the electron-beam write. Using the gold squares for alignment, the electron-beam writing system is capable of submicron alignment of patterns on the sample. The continuous grating was written in PMMA directly on top of the existing waveguides, as shown in Figure 19. As described previously, RIE was used to transfer the pattern into the silicon dioxide (Figure 20), and then into the $Al_xGa_{1-x}As$ (Figures 21 and 22). New thorough cleaning procedures for the RIE system insured clean and repeatable results between test samples and the real samples.
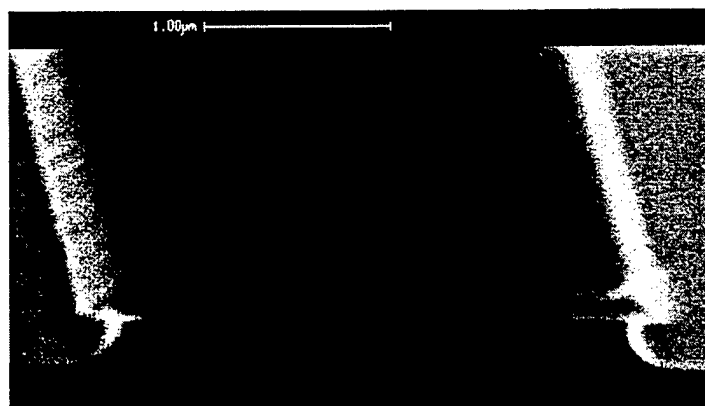

Figure 18. Cleaved facet of Waveguide 14 showing the effect of the 1:8:80 H_2SO_4:H_2O_2:H_2O etch. The silicon dioxide etch mask is still on top of the waveguide.
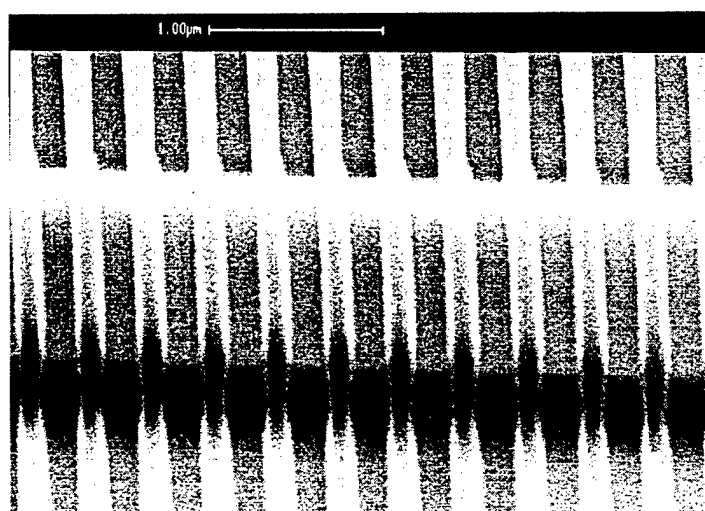

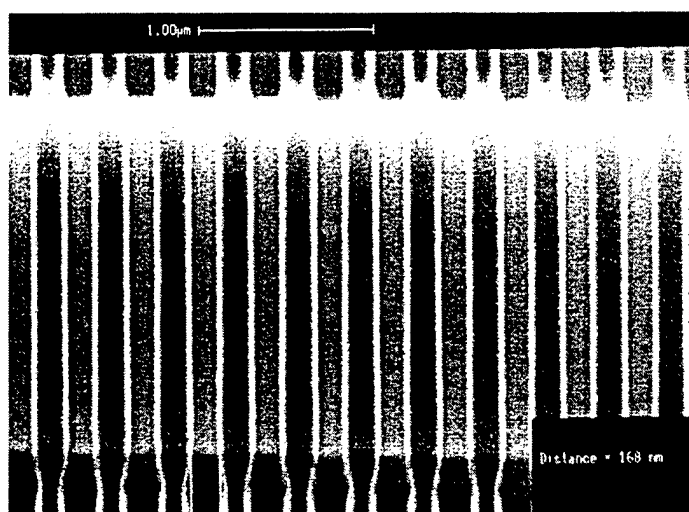**Figure 19. Grating written by electron-beam in PMMA on the waveguide.**

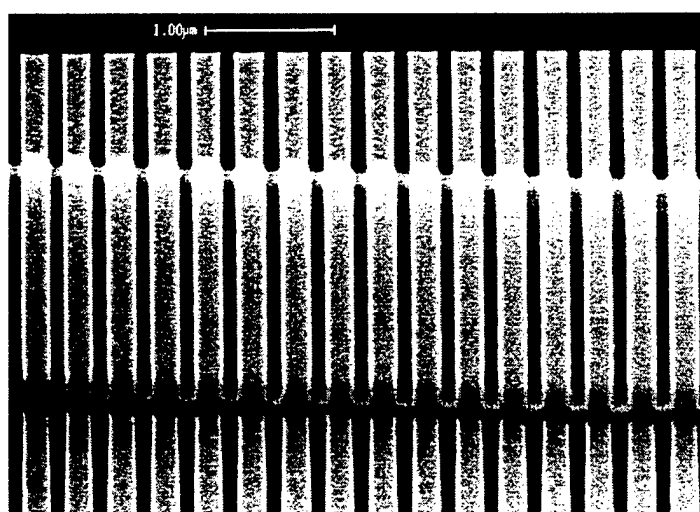**Figure 20. Grating etched into silicon dioxide.**

Figure 21. Grating etched into Al$_x$Ga$_{1-x}$As, top view.

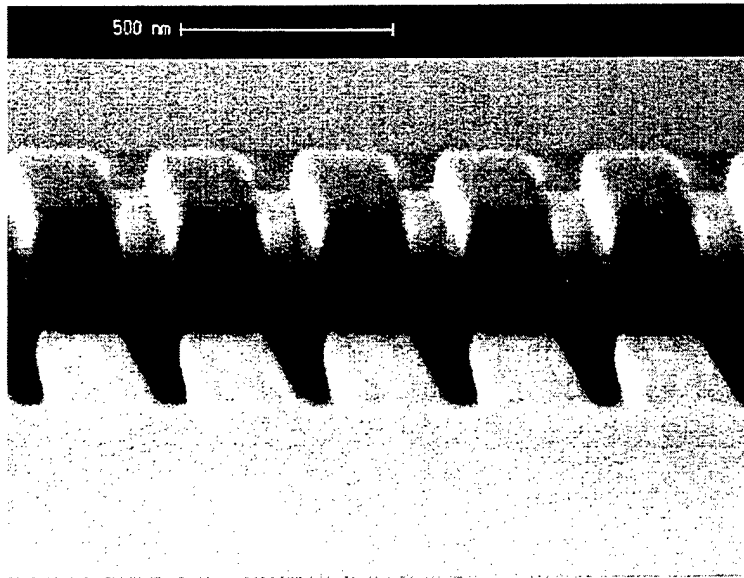**Figure 22. Grating etched into Al$_x$Ga$_{1-x}$As, side view.**

After the waveguide and gratings were etched, the remaining oxide was removed, and a 2.5 μm stripe was etched in a 1200 Å layer of silicon dioxide, as shown in Figure 23. Contacts were applied as described earlier. Figure 24 shows the contact on the waveguide. Figure 25 shows the completed distributed Bragg pulse shaper, and Figure 26 shows an uncleaved sample containing many pulse shapers.
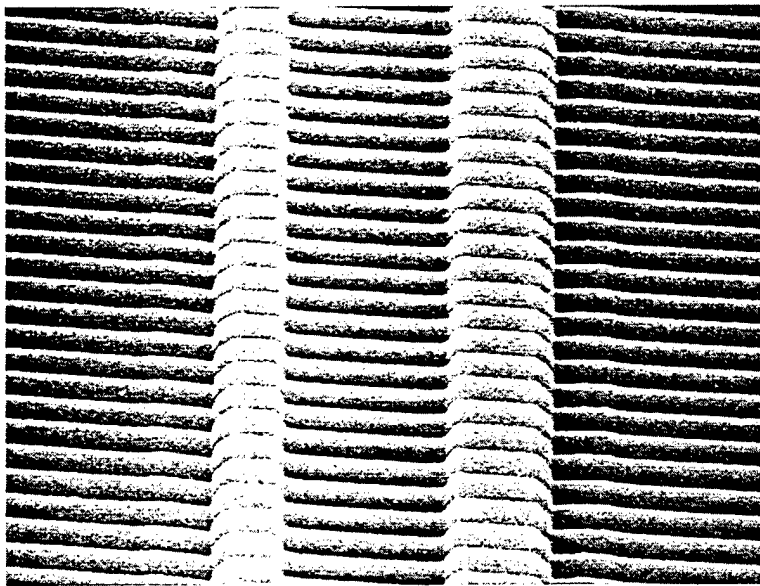

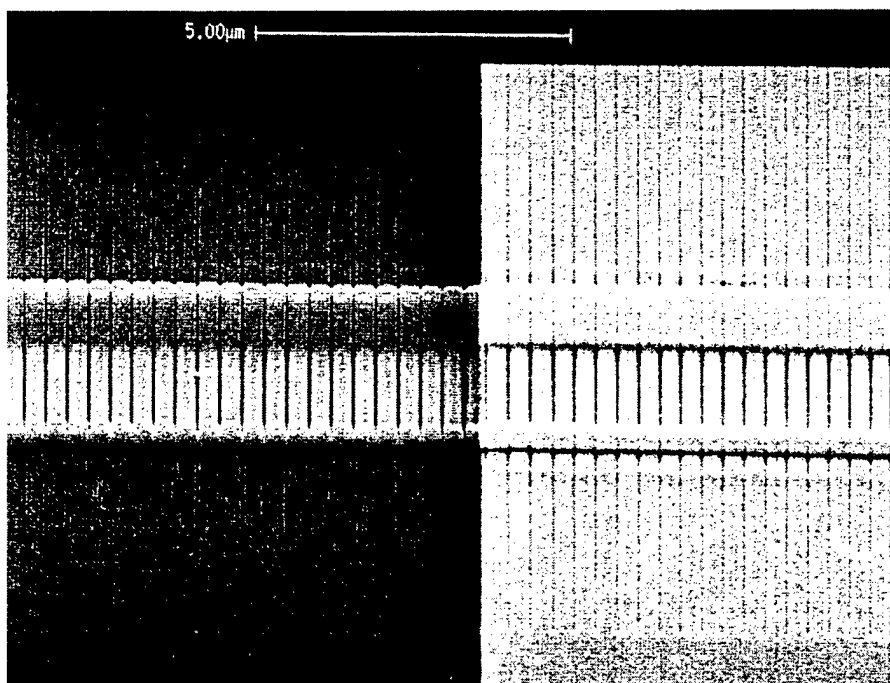**Figure 23. Contact window etched in silicon dioxide over the waveguide and grating.**
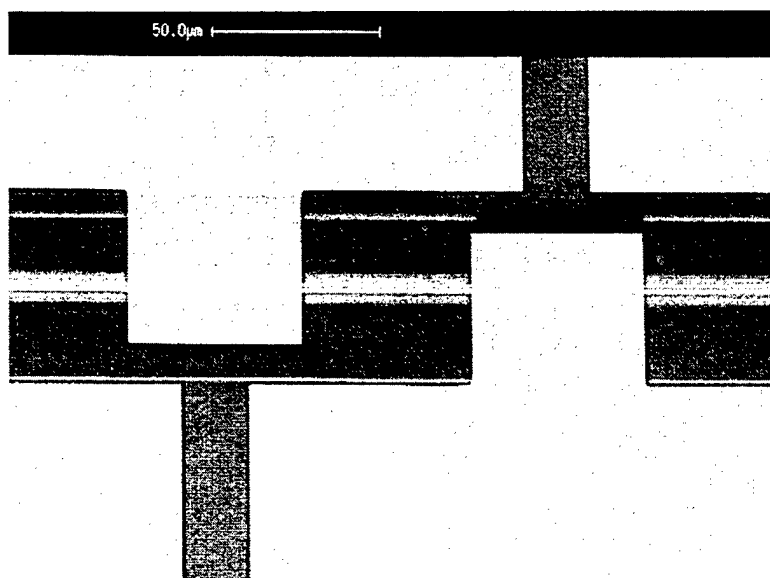
29

Figure 24. Grating with contact.

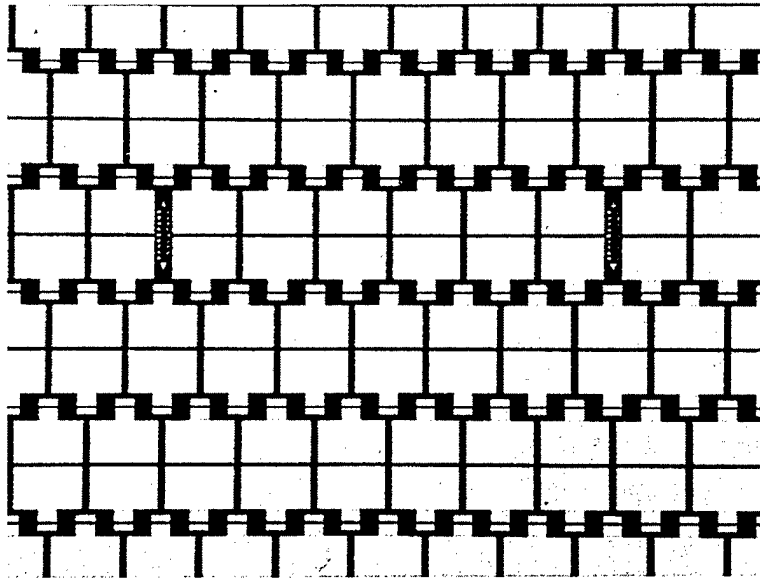**Figure 25. Distributed Bragg pulse shaper.**

Figure 26. Sample with many pulse shapers before cleaving.

A 50 μm long grating section is matched to an optical input pulse of approximately 300 fs. The Ti:sapphire laser used to test the devices is not capable of directly producing 300 fs pulses, so the 100 fs pulses from the laser are expanded in a single-ended Fourier plane pulse shaper before being launched into the waveguide, as pictured in Figure 27. In the Fourier plane pulse shaper, the beam from the laser is dispersed by diffraction off a grating. The beam is focused by a curved mirror onto the surface of a flat mirror. At this focal plane, the light is in a thin line, dispersed by wavelength. After the pulse is reflected from the flat mirror, it is again focused by the curved mirror back onto the grating, and recombined into a pulse.

Any filter placed in the focal plane of the system (at the flat mirror) will operate directly on the wavelength content of the pulse. A finite aperture, for example, with a square transmittance function, will multiply the optical spectrum by that square transmittance function. However, for testing the distributed Bragg pulse shaper, a square transmittance function is not desirable, because it creates a $\sin(t)/t$ temporal shape, which will cause crosstalk between reflections from successive grating sections. It is more desirable to create a roughly Gaussian spectral profile, which would also have a Gaussian shape in the temporal domain. Ideally, this could be done with special mirror in the focal plane with a Gaussian reflectivity function, but such a custom mirror would be expensive and difficult to fabricate. For these experiments, an adjustable slit was used near the curved mirror. This caused a transmittance function in an area where the spectral content of the beam was not focused, thus causing a roughly bell-shaped frequency transmittance function. Figure 28 shows examples of the spectrum of the laser pulse and the shaped pulses produced by the single-ended Fourier plane pulse shaper.
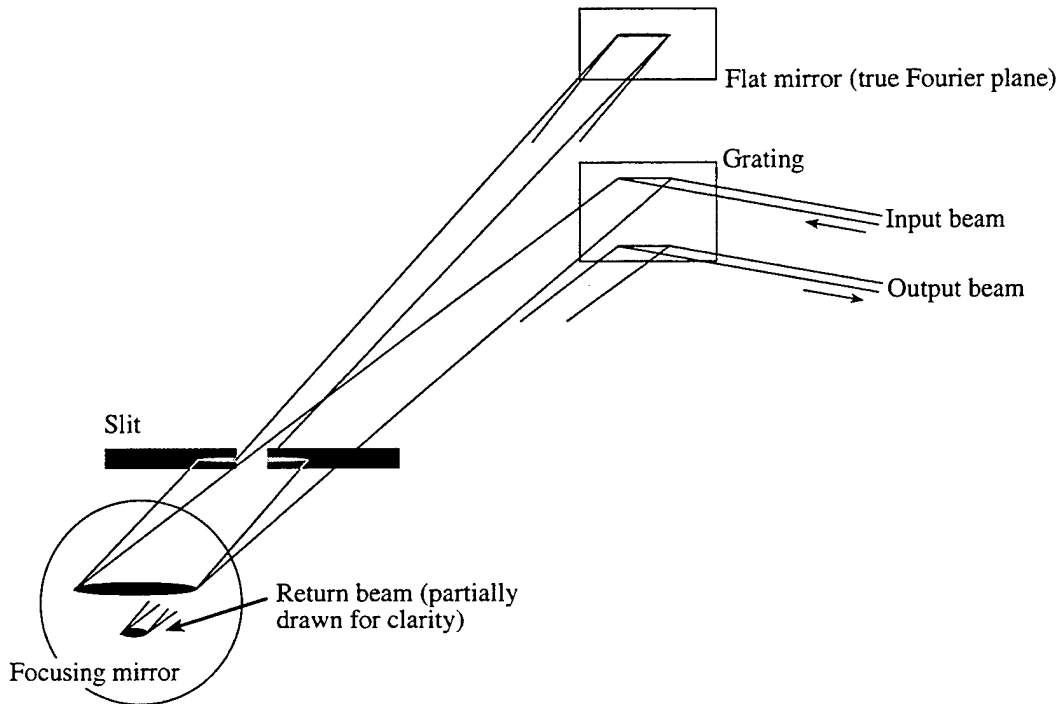
Figure 27. Single-sided Fourier plane pulse shaper. The slit is placed away from the Fourier plane to achieve a nearly Gaussian output spectrum.
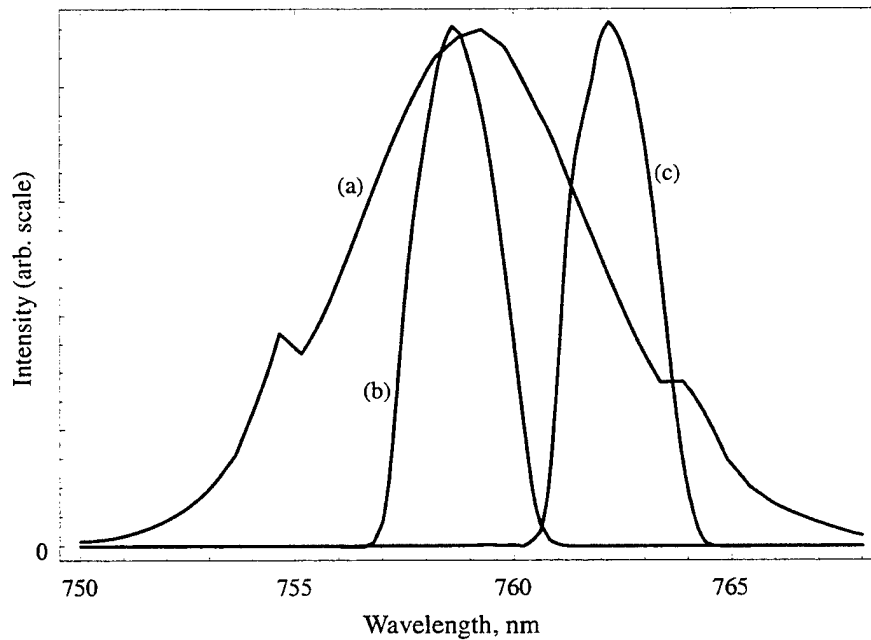

Figure 28. Spectra of laser pulse and shaped pulses. (a) Pulse from Ti:sapphire laser. (b) Shaped pulse at λ = 758.6 nm. (c) Shaped pulse at λ = 762.1 nm.

The test setup for Waveguide 14 is shown in Figure 29. A pulse from the Ti:sapphire laser is launched into the Fourier plane pulse shaper to modify the coherence length of the pulse. The shaped pulse is focused by a lens into the waveguide, and the front facet reflection is

blocked. Cameras above and behind the waveguide are used for monitoring alignment and light transmitted through the waveguide. A cube beamsplitter has replaced the two plate beamsplitters used previously, to reduce the effect of reflections from the antireflection coated faces of the plate beamsplitters, which produced many spurious fringes in earlier experiments. A variable neutral-density filter is used to adjust the reference beam intensity to be equal to the signal beam intensity for optimal fringe contrast. The reference beam is displaced upwards by a pair of mirrors, so as to produce horizontal fringes in the plane of the camera, and the camera is rotated 90 degrees, such that the fringes appear vertical. This is done because the data collection software relies on capturing a horizontal scan line across the screen.
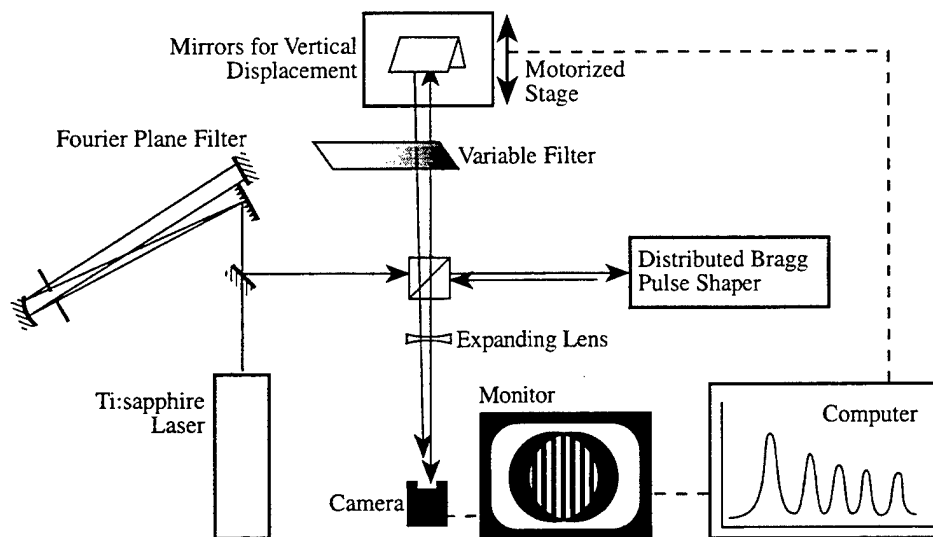

Figure 29. Test setup for Waveguide 14.

Figure 30 shows the signal beam at the plane of the camera. The beam is non-Gaussian for various reasons: The circular diffraction is due to the finite aperture of the focusing/collection lens. There are artifacts of linear diffraction due to the knife edge used to block the front facet reflection. The beam also is the result of light reflected and scattered from roughness and dust in the vicinity of the entrance facet, signal light emitted from the waveguide, and light coupled in to and out of the cladding regions adjacent to the waveguide. Although this beam quality is poor, a negative singlet lens is used to diverge this signal beam and the reference beam on the CCD camera, and smooth fringes can still be detected, as depicted in Figure 31.

Figure 30. Light from front facet of the distributed Bragg pulse shaper.
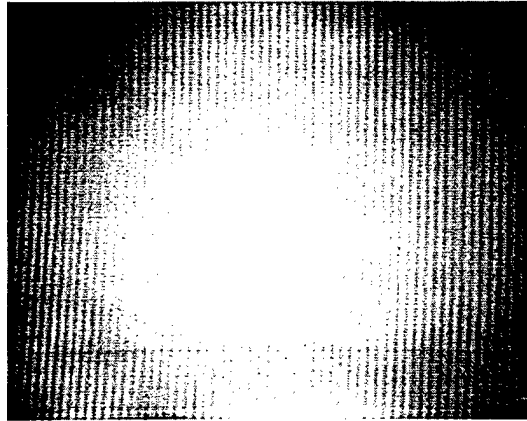
Figure 31. Fringes visible on the CCD camera monitor after expanding the output beam. The dark horizontal band is an artifact of the photo.

A computer is used to control the interferometer which detects the shaped packet produced by the distributed Bragg pulse shaper. This section will describe the computer program (written in C under MS-DOS) and the data collection algorithm.

A CCD camera is used to detect the fringes produced by interference between the output signal packet and the reference pulse. The camera is rotated 90° so that the interference fringes appear vertical on the monitor, and can be measured across a single scan line when digitized. The data collection program starts by digitizing a frame using an 8-bit frame grabber board, and displaying that frame on a TV monitor attached to the computer. A single scan line will be used for data collection, and the user is asked to select a line on the monitor. The computer displays a graph of the intensity across the scan line, and the FFT of that pattern to aid in selecting an appropriate location on the screen. After a line on the screen is selected, the user is asked to move the motor to a position where no fringes are visible. This is called the background position, and is subtracted from subsequent frames to measure the fringes. Figure 32(a) shows the background position, with the absolute measured intensity across the scan line in the lower trace, and the data enlarged in the upper trace. The user is then asked to move the motor to select a location with fringes, as shown in Figure 32(b). This frame shows the measured intensity in the lower trace, and the upper trace is the current frame minus the background frame, rescaled to fit the screen. When this location is selected, the subtracted data is Fourier-transformed, the user selects a filter type, and moves cursors to determine the width of the filter, as in Figure 32(c). A square filter is normally used, in which only one frequency component of the Fourier transform is selected.
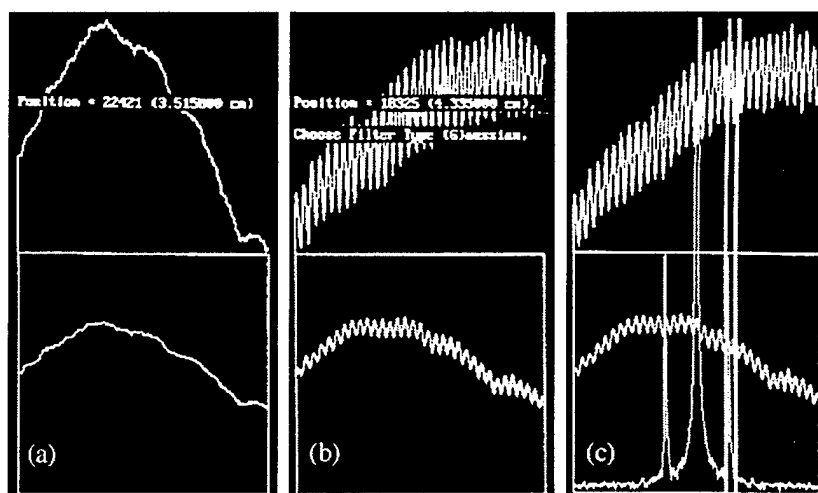
Figure 32. Example screens from the data collection program. (a) Shows a digitized scan line at the background position, (b) is at a position with fringes, and (c) displays the FFT of the fringes in the upper trace.

After selecting the screen position, background position, and filter width, the user provides an increment and start and stop positions for the motor, and selects how many screens will be averaged at each point and how many complete runs will be averaged. The program starts the data collection by averaging 10 captured scan lines at the background position, and normalizing the result. That is, each point across the averaged scan line, x'_n, is divided by the total integrated intensity of the scan line, $\sum_N x'_n$ and multiplied by N, the total number of points. This normalization allows canceling of laser noise between frames.

The computer moves the motor to the start position and collects data as follows: At each motor position a scan line of points x_n is captured. The scan line is normalized (again by dividing by each point by the total intensity), and the normalized background data is subtracted. This gives the vector

$$g_n = \frac{N\,x_n}{\sum_N x_n} - \frac{N\,x'_n}{\sum_N x'_n} \tag{3.1}$$

This vector is Fourier transformed using an FFT algorithm. Because the fringe data is real, the FFT is symmetrical. The magnitude of the points in one half of the symmetrical FFT are multiplied by the filter function, and integrated over all frequencies. The computer displays a graph of this integral at each motor position and the FFT at the current motor position. In most cases, the filter is a square filter, one point wide in the FFT, so the result of this operation is simply to provide the intensity of the FFT at that frequency. A sinusoidal fringe variation of amplitude d will produce two peaks in the FFT of amplitude $dN/2$, where N is the total number of points. Dividing this result by $N/2$ gives the fringe visibility $v_n = 2\,g_n / N$ at the current motor position.

The term fringe visibility $V(\mathbf{r})$ at a point $P(\mathbf{r})$ in an interference pattern was introduced in 1890 by Michelson as

$$V(\mathbf{r}) = \frac{\langle I \rangle_{max} - \langle I \rangle_{min}}{\langle I \rangle_{max} + \langle I \rangle_{min}} \qquad (3.2)$$

where $\langle I \rangle_{max}$ and $\langle I \rangle_{min}$ represent the maximum and minimum values of the averaged intensity in the vicinity of P. Upon comparison it can be seen that the quantity measured by the algorithm is equivalent to the average fringe visibility across the captured scan line.

Consider signal and reference pulses, each with intensity I_0. At a given path length difference (i.e., motor position), the reference pulse will interfere with any component of the signal pulse that is within one coherence length. If the fraction of the power in the signal pulse that will interfere has intensity I_s, the remainder of the signal pulse has intensity $(I_0 - I_s)$. The signal at the screen is the sum of this noninterfering part with the interfering part. This signal has maximum and minimum values

$$\langle I \rangle_{max} = (\sqrt{I_0} + \sqrt{I_s})^2 + (I_0 - I_s) = 2I_0\left(1 + \sqrt{I_s / I_0}\right)$$
$$\langle I \rangle_{min} = (\sqrt{I_0} - \sqrt{I_s})^2 + (I_0 - I_s) = 2I_0\left(1 - \sqrt{I_s / I_0}\right). \qquad (3.3)$$

Inserting these equations into (3.2) gives the simple result for the fringe visibility

$$V(\mathbf{r}) = \sqrt{\frac{I_s}{I_0}}. \qquad (3.4)$$

This shows that the fringe visibility that is measured is proportional to the square root of the intensity in the pulse, and thus proportional to the magnitude of the electric field.

One bar cleaved from a sample of Waveguide 14 was mounted in the high speed mount discussed above. This particular device is called 14.1T1.H1, Device 8. A wirebond was made directly to the second contact pad on the device, as pictured in Figure 33. An I-V curve of the device, in Figure 34, verified ohmic contacts and a good p-n junction.
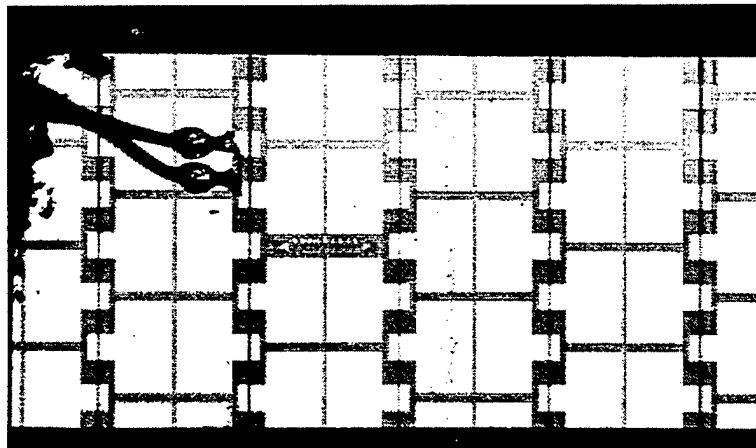

Figure 33. Cleaved and mounted device with two wire bonds on one contact.
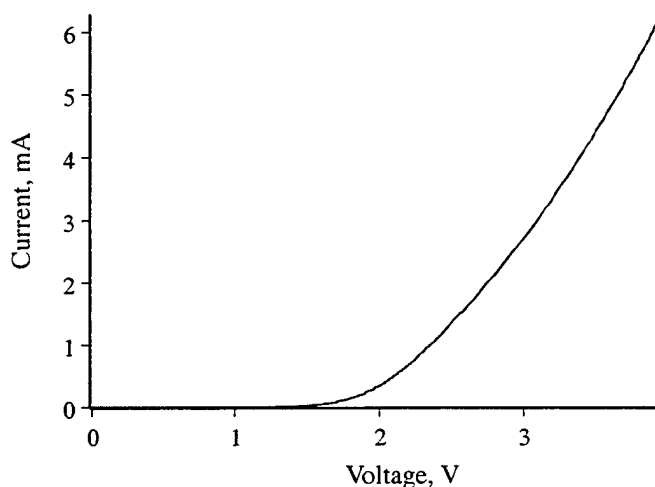
Figure 34. I-V curve for 14.1T1.H1, Device 8.

The distributed Bragg pulse shaper was tested to determine the resonance wavelength of the sections of Bragg grating. Light was launched into the pulse shaper, and the motor was positioned such that the reference pulse would interfere with the component of the signal pulse generated by a desired grating on the device. The wavelength of the input light was then scanned by tuning the Ti:sapphire laser and Fourier plane pulse shaper, to find the wavelength at which interference fringes were produced. It was found that the sections of grating with 346 nm and 333 nm periods reflected wavelengths of 780.1 nm and 758.3 nm respectively. This is 3.2% and 3.1% lower than the expected values of 806 nm and 783 nm. This is a result of error in the calculation of the dependence of the refractive index on aluminum concentration, and in the estimation of the effective index of the waveguide modes. Similar errors are observed by others in Prof. J. J. Coleman's group at University of Illinois in the design of DFB and DBR lasers.

Operation of the distributed Bragg pulse shaper was demonstrated for the two different modes of operation: normally-on, and normally-off. For the normally-on case, the Ti:sapphire laser and Fourier-plane pulse shaper were set to produce pulses of wavelength of $\lambda = 758.6$ nm with a full width at half maximum (FWHM) of $\Delta\lambda = 2.2$ nm, as shown in in Figure 28. The shaped pulses were launched into the distributed Bragg pulse shaper and the shaped packet was measured using interferometric cross-correlation. This measurement was performed with no current, and repeated with dc currents of 5 mA, 10 mA, and 25 mA injected into the second grating of the device. The resulting waveforms are shown in Figure 35 and Figure 36. The first large pulse is a result of strong reflections from the front facet. The following pulses are reflections from segments of grating. The spacing of the reflections suggests the pulses travel in the semiconductor with a group index of $n_g = 4.1$.
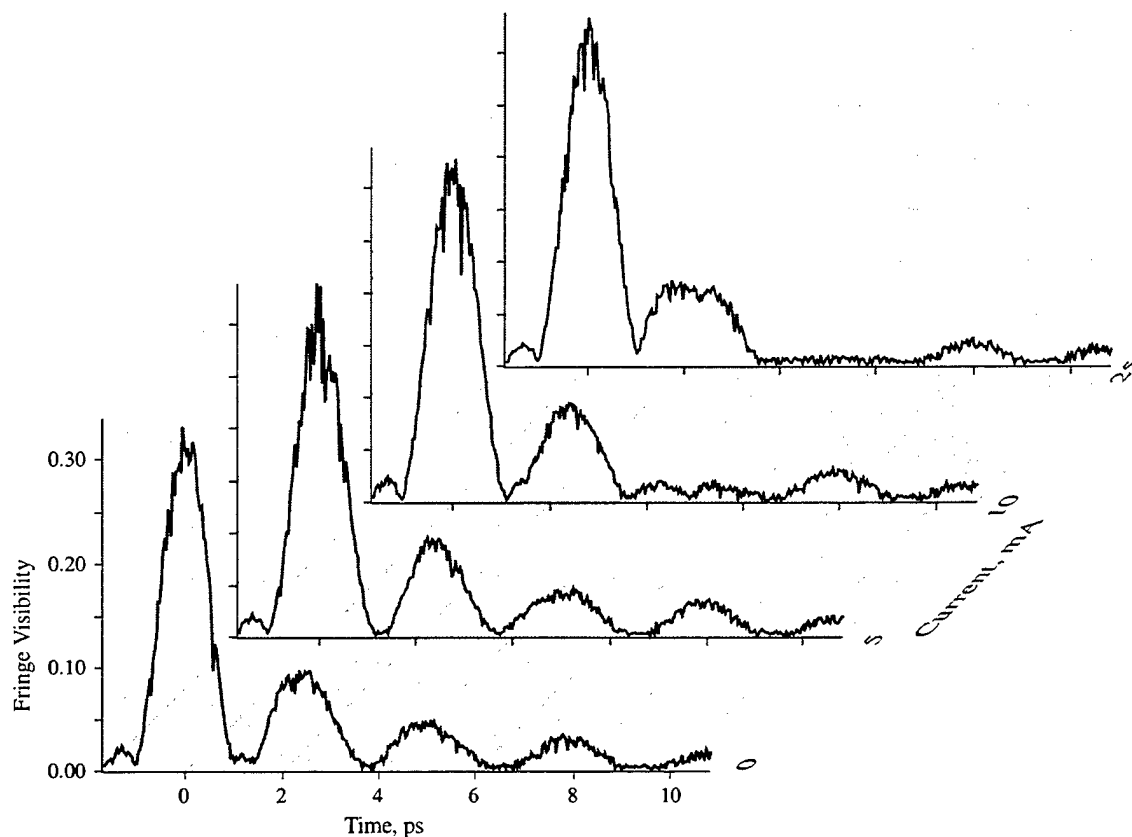
Figure 35. Normally-on operation of the distributed Bragg pulse shaper. Increasing current switches off the reflection at time $t = 5$ ps.
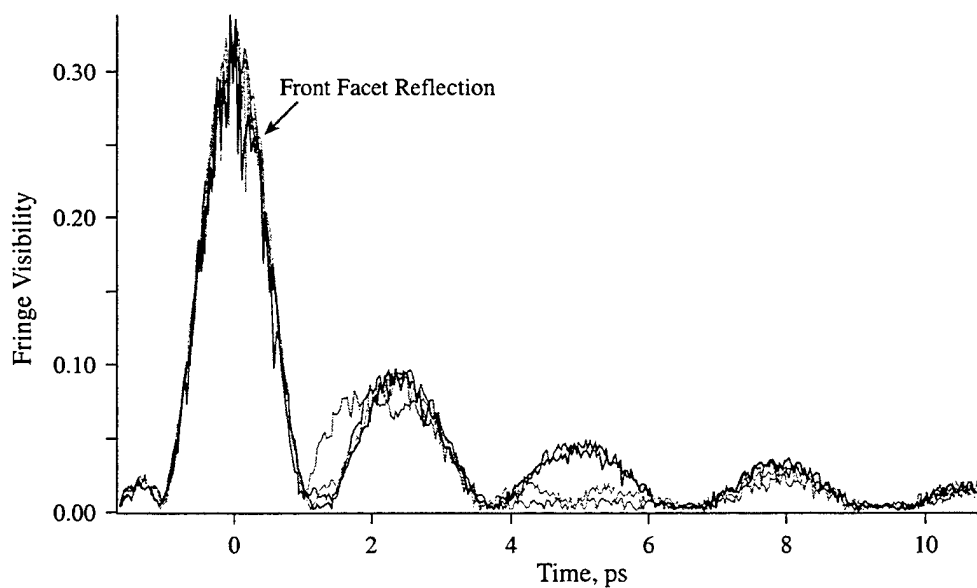

Figure 36. The four curves above superimposed.

For the normally-off case, the Ti:sapphire laser and Fourier-plane pulse shaper were set to produce pulses of wavelength of λ=762.1 nm with a FWHM of $\Delta\lambda$=2.2 nm, as shown in in

Figure 28. The shaped packet was tested with no current, and again with 17.5 mA dc current to turn on the reflection from the grating section. The data are presented in Figure 37.
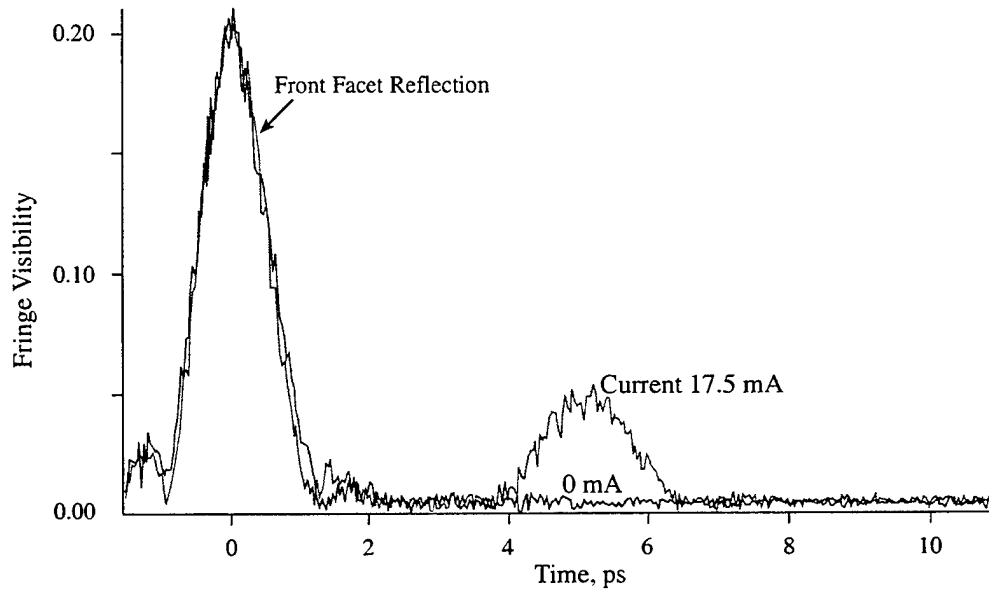

Figure 37. Normally-off operation of the distributed Bragg pulse shaper. Increasing current switches on the reflection at time $t = 5$ ps.

It was possible to measure the refractive index change produced by the injected current in two different ways. In the first, the peak reflection wavelength of the Bragg grating was found as a function of input current. In the second method, the phase shift of light passing through the grating section was measured as a function of current.

To measure index change, the motor was positioned to detect interference fringes from the grating with the wire-bonded contact (a grating section with 333 nm period). The laser and Fourier plane pulse shaper were tuned to find fringes of peak visibility. Then a range of dc currents were applied to the grating section and the wavelength at which peak fringes were detected was recorded. Figure 38 presents the measured grating resonance as a function of electrical current.
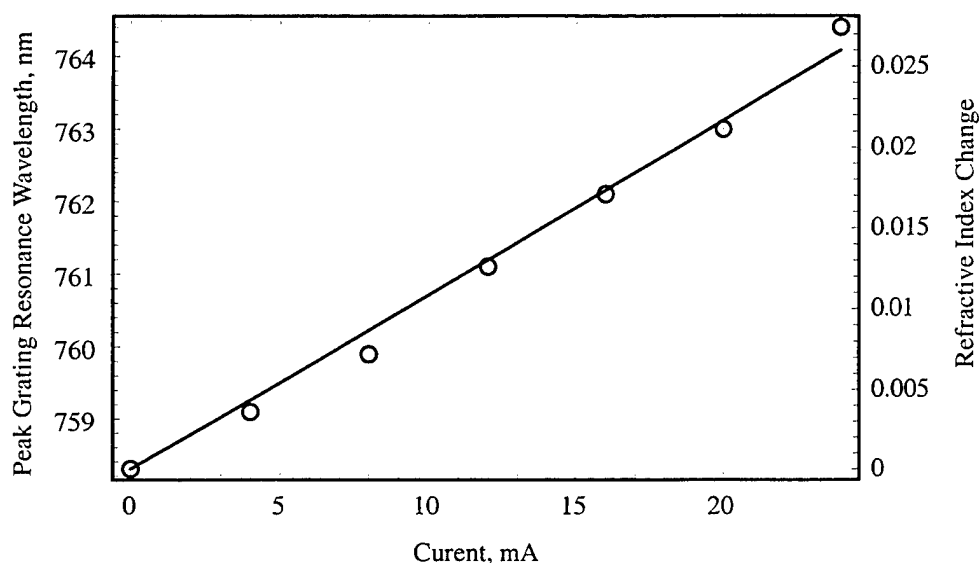
Figure 38. Measured peak grating resonance wavelength and calculated effective refractive index change as a function of current applied to the grating section.

The effective index n_{eff} is related to the third-order grating period Λ and the wavelength of peak reflection λ by the relation

$$n_{eff} = \frac{3\lambda}{2\Lambda} \qquad (3.5)$$

so the change in effective index induced by the injected current can be calculated from the shift in grating resonance, and is also presented in Figure . A linear fit to the data, also pictured on the curve, gives the relation $\Delta n = 1.08 \, 10^{-3} \, i_g$, where Δn is the change in refractive index, and i_g is the dc current in the section of grating. Assuming the current and index change mechanism are well confined under the 50 µm × 3 µm area of the contact, the current density causes index change $\Delta n = 1.63 \, 10^{-3} \, J$, where J is the current density in kA cm^{-2}.

The positive sign of the measured refractive index change suggests that the index change observed is a result of thermal effects (of positive sign) in the material overshadowing free carrier plasma effects (of negative sign).

The electrically induced change in path length was used to estimate the group refractive index change observed in Waveguide 14. The reference motor was positioned such that interference fringes were visible on the monitor resulting from light that had traveled through the electrically contacted grating segment and was reflected by the segment beyond it. The phase shift $\Delta\phi$ of fringes on the screen was measured as a function of the input current. The direction of the motion of the fringes as a result of increasing dc current indicated an increased index, confirming the sign of the index change measured above. The index change is presented in Figure 39, and is calculated from the path length change in two transits through the 50 µm section where current is injected. This gives a change in the group index of

40

$$\Delta n_g = \frac{\lambda \, \Delta\phi}{2 \, 50\,\mu m} \, . \qquad\qquad (3.6)$$

A quadratic fit to this data gives the relation $\Delta n_g = 7.70 \, 10^{-4} \, i_g + 2.50 \, 10^{-5} \, i_g^2$, where Δn_g is the change in refractive index, and i_g is the dc current in the section of grating. For the index change calculations, it is assumed that spreading of current and refractive index change mechanism are negligible, such that the measured phase shift occurs only in the section of the waveguide that is covered by the 50 μm wide contact. Figure 40 shows the spontaneous emission from the device when pumped with 20 mA of current. The highly localized nature of the spontaneous emission confirms that the current stays well confined.
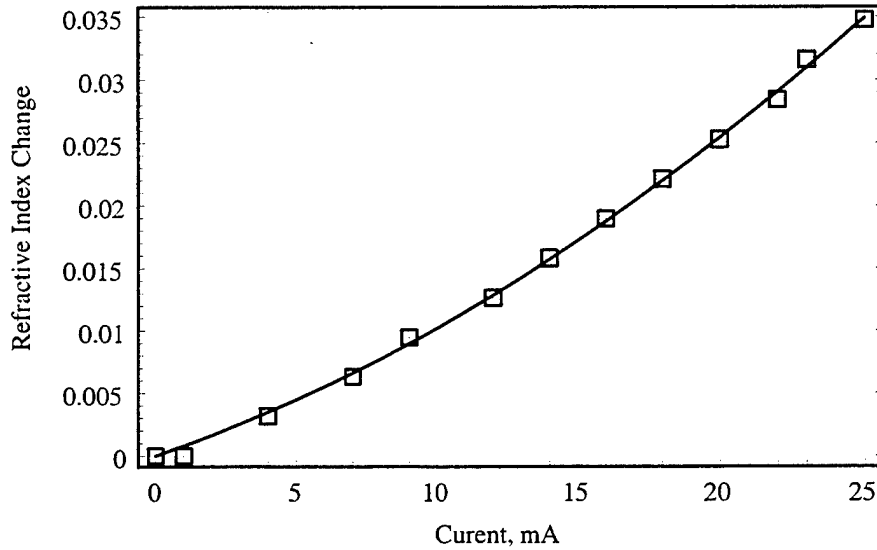

Figure 39. Measured maximum group refractive index change as a function of current applied to the grating section.

Figure 40. The distributed Bragg pulse shaper in operation. Light is injected into the facet at the left. Current in the grating section causes spontaneous emission.

41

The Quantum Dot Spectrometer

The Distributed Bragg Pulse Shaper provides an efficient means of turning parallel electrical signals into an ultra-fast optical signal, but does not provide an immediate solution to the reverse problem of turning an serial optical signal into a parallel electrical signal. We have developed two methods for this reverse transformation: spectral disparity and spatial disparity sensors. A spectral disparity sensor using spectral sensitivity to separate channels in a point detector. A spatial disparity sensor separates spectral or temporal channels in space. The general idea of spectral disparity sensors is represented in spectral hole-burning materials. With the quantum dot spectrometer, we add electrical addressing to the capacity of hole-burning.

Under this program, we implemented the simulations and experiments on an electrically-tunable spectrally-sensitive photodetector based on inhomogeneous absorption in a self-assembled quantum dot array and resonant tunneling through a coupled quantum well layer. The basic structure of our device, the quantum dot spectrometer (QDS) is sketched in figure 41. The key components are the quantum dot layer, which produces spectrally sensitive absorption and the coupling layer, which reads out spectral information as a function of the applied voltage, V.
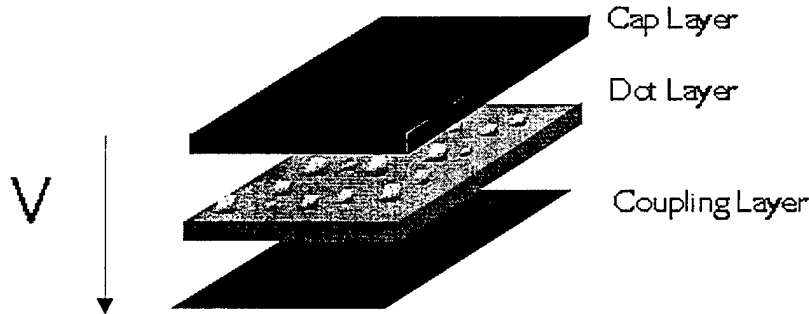
Figure 41. Structure of the quantum dot spectrometer.

The coupling layer consists of a pair of coupled quantum wells. For certain applied bias voltages across the quantum wells, resonant transfer from the quantum dot layer to the collector layer will occur. Specifically, resonant transfer occurs when the following conditions are met:

$$E_{dot} = E_{qw1} + \frac{\hbar k_\parallel^2}{2m_1} + \alpha_1 V$$

$$E_{dot} = E_{qw2} + \frac{\hbar k_\parallel^2}{2m_2} + \alpha_2 V$$

where E_{dot} is the electron energy in the quantum dot, E_{qw1} and E_{qw2} are the energies of the electron states in the quantum wells, $k_\parallel$ is the electron momentum parallel to the layer interfaces,

α_1 and α_2 are geometry dependent constants and V is the applied voltage. Two quantum well layers are necessary to force the two free parameters $k_{\parallel}$ and V to assume unique values for each electron energy level in the quantum dots. The applied voltage which couples photo-excited charge out of a particular dot energy, E_{dot}, is

$$V(E_{dot}) = \frac{m_1(E_{dot} - E_{qw1}) - m_2(E_{dot} - E_{qw2})}{\alpha_1 m_1 - \alpha_2 m_2}$$

For the readout voltage to depend on the dot energy, the effective masses of the two quantum wells must be different. This is achieved by using different materials compositions in the quantum wells.

We have constructed a preliminary device based on these concepts using the InAs-GaAs-AlAs material system. Figure 42 shows photoluminescence data from this device. The characteristically broad inhomogeneous dot luminescence is apparent in the figure. Figure 43 shows the I-V response of the device at three different wavelengths. While we are encouraged by this demonstration of electrically-tuned spectral sensitivity, considerable further efforts are needed to narrow the spectral response and improve the quantum efficiency.
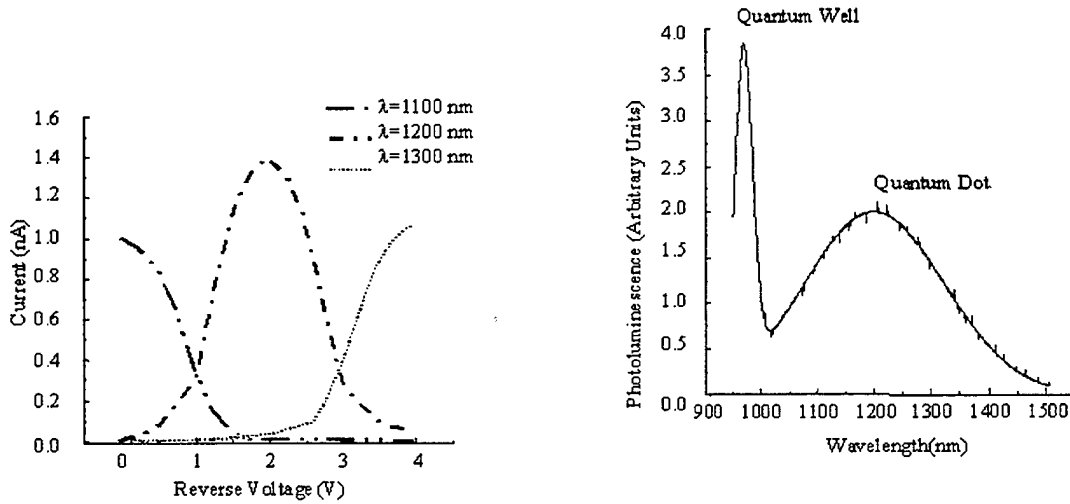
Figure 43. I-V response for the QDS.

Figure 42. Photoluminescence of a QDS structure.

While we were able to demonstrate spectrally sensitive absorption with this first generation device, several challenges remained. Most notably, the quantum efficiency is low fundamentally low in devices based on a single layer of quantum dots and this efficiency is further reduced by simplex detection of a single spectral channel. Furthermore, the native spectral range of a self-organizing dot layer in the near infrared is relatively limited. This proposal dramatically

improves this situation by proposing multiplex dot detectors which fully utilize all absorbed photons, by proposing to use intrasubband transitions in the mid-IR to obtain useful spectral range, and by proposing a relatively simple device architecture consistent with multiple dot layers.
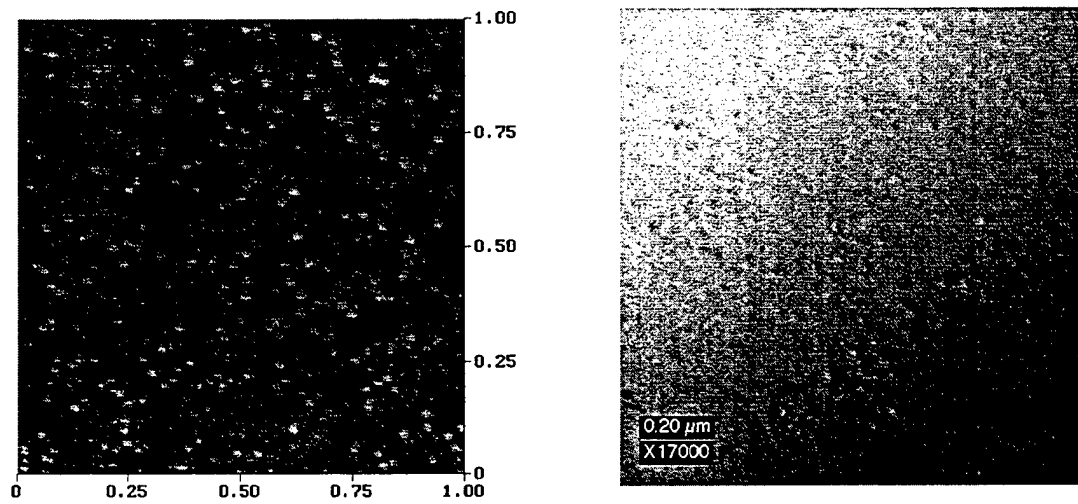

Figure 44. AFM and TEM image of fully coherent quantum dots grown at UIUC

Next generation devices will be based on atmospheric pressure MOCVD growth of high quality, high density quantum dots. We have the ability to grow fully coherent, optical quality InAs dots on GaAs via APMOCVD (Fig 44). The advantage of APMOCVD is that is a technology easily transferable from research to production lines, giving a relatively fast turnaround in terms of proof-of-concept devices to manufacturable status. This InAs-InGaAs/GaAs system allows us to access the wavelength detection regimes of 1 um to 1.3 um for interband transitions and 8-12 microns with intraband transitons. Since detection wavelength of the dots depends on both the size and the composition of the dot, we would first work on understanding how these parameters affect the properties of the dots so that we can easily access, control, and widen the bandwidth of detectable wavelengths. Along with the PL and CL measurements of our QDs, it is also essential to perform transmission electron microscopy (TEM) using a novel strain field technique in order to determine the factors contributing to density and composition of these QDs.

By varying growth conditions such as growth rate, growth temperature and deposition time, we are able to grow a high density of coherent InAs dots around 7 nm in diameter. The deposition thickness window to obtain fully coherent, defect free islands required the deposition thicknesses to be between 0.96 MLs and 1.52 MLs with a maximum density of ~4.7x10^{10}cm^{-2} at 1.31 MLs. Figures 1 and 2 display AFM and TEM images of the coherent dots at the optimal ML coverage of 1.31 MLs. The AFM shows the distribution of the dots on a 1 μm area. The dots appear randomly distributed and have an approximately gaussian size distribution centered around 7 nm.

High quantum efficiency devices require multiple dot layers. Figure 45 shows a cross-section of a quantum dot array of 30 individual layers of InAs quantum dots imbedded within a GaAs matrix. The layers are separated by 1 nm GaAs, and the InAs dots in this figure are roughly 5 nm in size. This size shows very little st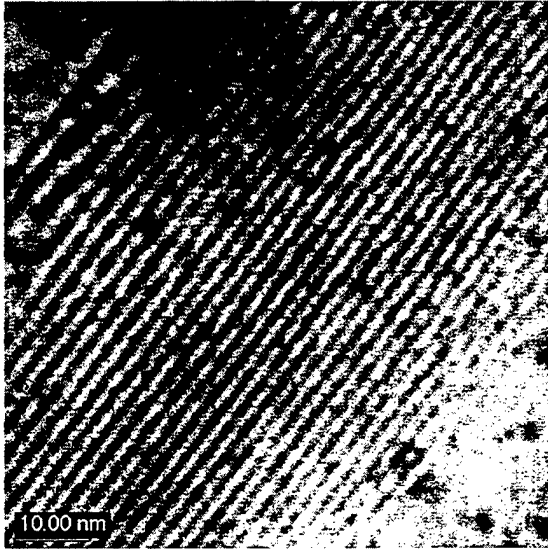rain field interaction with the rest of the matrix. This growth method allows us to create dot layers that are independent in position with the other dot layers. By increasing the deposition thickness, we can strain-couple dots between layers in order to make vertical stacks, thus giving us the ability to tailor our dots to whatever specification we choose.

Quantum dot stacking is a technique used in order to increase the effective density of dots per unit area, thus increasing the sensitivity of the active detection layers. We are already able to generate dislocation-free stacks of InAs dots, and so the focus of this project phase would be to learn how multistacked layers of arbitrary dot parameters are coupled to InGaAs quantum wells. We would then move on to multistacked layers with different sizes and compositions of dots. Therefore, optimization of the quantum transfer efficiency of these dots to the wells as well as bandstructure design will be the primary focus of this project phase. This will allow us to tailor our materials and devices to the demands and specifications of the program. At the device level, collaborative efforts with the industry will be needed in order to test and characterize the abilities of the devices.

Figure 45. Multistacked Epitaxial Growth

The design of multi-layer dot structure for a new class of high functionality photo-detectors will be primarily achieved by the implementation of large scale CAD tools capable of simulating realistically the quantum dot structure in their environment of dopants and hetero-layers under strain. We will use comprehensive and powerful 3-D computer models for the analysis of the electronic and optical properties of quantum dots. University of Illinois 3D codes have the unique capability of incorporating all the quantum mechanical, statistical, electro-dynamical and structural features of nanosystems with arbitrary geometry in a self-consistent fashion. This realistic approach has been most successful for the computation of the electronic spectra and charging effects in pyramidal self-assembled InAs/GaAs QDs. The Local Spin Density Approximation (LSDA) accounts for spin effects, coulomb interaction and shell filling in these artificial atoms.

By capitalizing on discrete state absorption and polarization sensitive intra-band selection rules, semiconductor quantum dot structures provide a unique opportunity to build detectors capable of capturing the full information content of the field. Using self-assembled quantum dot (SAD) detection layers enable point photo-detectors that fully analyze the hyperspectral structure or the polarization distribution of the field. The idea relies on the following observations:

a) SADs sizes and composition can be varied within certain limits, and can therefore be engineered to provide particular carrier confinement with particular energy spectra; in other terms, the SAD electronic properties can be tailored for specific electronic and optical functions.

b) Three-dimensional confinement in SADs induces selection rules for optical transitions between conduction band states as a function of the dot geometry.

c) Slow carrier relaxation by phonon-assisted scattering occurs in highly confined SADs as a result of the restriction on available discrete electron states, unlike in bulk semiconductors or QWs which display an energy continuum. SADs are therefore characterized by longer retention times for excited electrons on upper energy levels, which provides new opportunities for retaining the information associated with the electron excitation.

Figure 46. Schematic representation of field ionization from the multi upper levels of a quantum dot sandwiched between two modulation doped barriers. The upper dark lines are for low field; The lower lines are for high field

d) The combination of longer retention times with a inhomogeneous spectral distribution of levels which results from non-uniformities in SAD sizes, offers also opportunities for spectrally sensitive detection over wide ranges of optical wavelengths. The property has recently lead to our proposal of a new class of detectors with multi-spectral capability, the Quantum Dot Spectrometer (QDS).

As a particularly promising system for new photo-detector functionality, we propose a modulation doped multi-layer quantum dot structure. This device uses the naturally broad absorption spectrum of inhomogeneous self-assembled quantum dots to capture multiple wavelengths and field ionization tunneling to generate electronic signals proportional to the power at specific wavelengths. The multi-layer structure enhances the absorption responsivity,; in addition, variations of the layer width, dot size and doping between layers provide additional degrees of freedom to increase inhomogeneous spectral broadening.. Field ionization by an external potential will selectively extract photo-excited carriers for the electrical signal as recently demonstrated. Materials composition (e.g. InAs/GAs vs InGaAs/AlGaAs), structure configuration (layer periodicity and doping) and design structure (insertion of variable bandgap
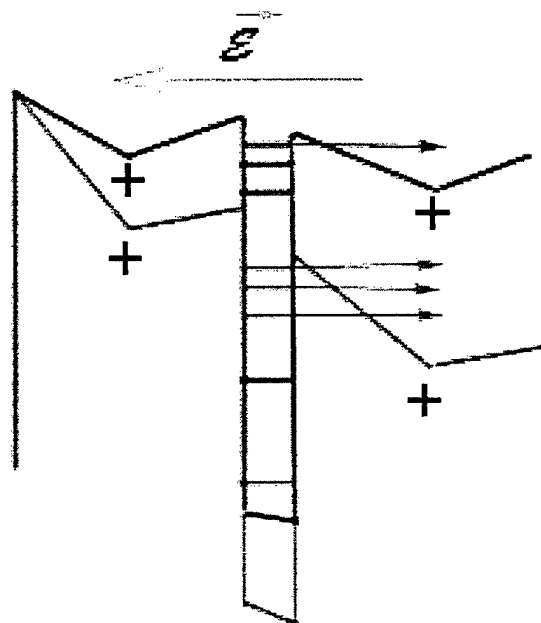
quantum wells to resonantly bridge between dot layers and enhance responsivity) will be investigated to optimize device performances. For this purpose, we will develop efficient software models capable of simulating the static and the dynamics of quantum dots in the multi-layer modulation doped structures . The key goal to the function of this device is to achieve the relatively high quantum efficiency of the multilayer approach without losing the spectral selectivity of homogeneous absorption. This goal will be achieved by applying multiplex concepts at the lowest level of device function. Modulation of layer widths and barrier combines the spectrally random layer responses in variable projections. By analyzing the device response under a variety of applied fields, we can invert against a calibrated response to find the incident spectrum. This approach achieves much better quantum efficiency and is much simpler to fabricate than our earlier resonant tunneling spectrometers.

While our near term goal is simply to demonstrate high resolution spectral analysis in dots, investigation of quantum dots for functional focal planes will lead over the longer term to extra-ordinarily sophisticated detectors. Using selective Area epitaxy (SAE), one may eventually create multiple devices operating on different wavelengths grown simultaneously, giving a "lab on a chip" concept to photonic detection systems. SAE enables growth of epitaxial layers on selected regions of a wafer. This technique employs a growth inhibition dielectric mask of SiO_2 or SiN_x patterned on a substrate by conventional photolithography. This method allows growth to take place only on the unmasked regions. SAE is another novel technique to further modify and control the underlying strain field that affects the QD characteristics.

Interferometric Sensors

This program focused on encoding and detecting dense information on optical fields. We showed how volume holograms can be used to encode and analyze complex space-time field patterns [8, 11, 13] and how interferometric receivers can decode these patterns [14, 15] . This work was primarily targeted at ultra-fast communications and processing applications. Ultimately, it led to the development of specialty compound semiconductor devices, such as the distributed Bragg pulse shaper [16] and the quantum dot spectrometer [17]. Throughout this work, phase sensitive detection has been shown to be enabling of important capabilities, as in our demonstrations of coherence multiplexing [18], of ultra-fast pulsed image analysis [11] and in our demonstration of polychromatic microscopy [19]. We have shown that optical fields can contain substantially more information at higher bandwidths than conventional systems predict. As an extreme example, we showed that space-time control of homogeneous quantum systems could create sub-wavelength spatial excitation patterns [20].

Over the final year of the program, it became apparent in our work on interferometric space-time communications that the sensor models we were developing had profound implications for imaging systems. With the growing maturity of communications markets and the increased need for reliable and powerful interfaces between information hardware and the physical world, research into the imaging applications of these devices has become increasingly essential.
The primary difficulties with analog processing in imaging systems are that the measurement and reconstruction spaces must be isomorphic and that mappings onto physical spaces create information bottlenecks. The isomorphism problem is illustrated by the fact that the reconstruction spaces for conventional imaging is 2D because the measurement space is 2D. The

bottleneck problem is illustrated by the fact that conventional wavelength and spatial imaging uses measurement and reconstruction spaces with as many degrees of freedom as the source domain, resulting in unreasonably high data loads. The isomorphism and bottleneck problems are avoided by separating the functions of imaging systems in design. The field should be viewed as a channel through which the source communicates with the sensor system. The goal of the physical system is to maximize the **relevant** source information communicated through this channel. (The relevance of source information is controlled by adapting the channel based on channel analysis and observer feedback.) A well-designed system separates source reconstruction and modeling from data acquisition. A well-designed system also considers the source in its native space.

Multi-dimensional source reconstruction is desirable for many reasons, but the most compelling is that discarding 3D, 4D and 5D relationships between reconstruction points inevitably wastes information resources. A static scene captured as a stream of video data from a moving sensor is more compactly represented as a 3D scene. While a human watching the video sequence can infer the 3D structure, why should they serve as the reconstruction processor? The scene reconstructed in its native form can be reprojected arbitrarily to human and machine observers. Similarly, a scene changing in time or in spatio-spectral time should be represented in a 4D or 5D space optimized for compact respresentation. The point is that a system should manage data streams in an informed and application specific manner with user feedback. This approach is not possible with analog processing, but is natural to digital systems.

By definition, a system in with no isomorphism between the object space and the measurement space is a multiplex system. As mentioned above, the most common type of multiplex imager is the imaging Fourier transform spectrometer. Rotational shearing imagers (RSI), however, demonstrate that the multiplex principles of FTS spectroscopy can be generalized. The FTS and RSI systems are "interferometric imagers," which normally is taken as a synonym of "multiplex." However, all imaging systems are in some sense "interferometric." The trick is to design the beam combining elements of the interferometer to maximize information transfer. Optimal designs will be target dependent, however, so adaptive optical components are needed.

Dramatic improvements in embeddable processors and electronic sensors in the past 5 years are revolutionizing the design of visible and infrared imaging systems. Traditionally, optical imaging is viewed as the process of creating 2-D field distributions that are visually similar to 3-D objects. In the emerging paradigm, imaging is the process of gathering digital information to model objects in three or more dimensions. The basis emerging opportunities is reliance on digital processors to extend or even replace transformations due to analog imaging components, such as lenses and mirrors. Despite this shift, imaging remains a fundamentally analog process at the interface between the physical world and the modeling system. Optimal design of the analog optical components for imaging systems is a significant and unresolved problem in the context of digital imaging.

Computation in incoherent imaging has typically relied almost completely on the optical system, leaving little work for the sensor. Lens-based imagers work only for sources with a limited range of depth. For imaging volume sources, a lensless optical system in conjunction with

digital data synthesis may perform better. In particular, measuring the coherence of the field with a Rotational Shearing Interferometer (RSI) [21-25] can provide superior performance over a large range of depth, because a depth-invariant representation of the field can be prepared optically for electronic sensing and computation.

Consider a three-dimensional incoherent source imaged with a lens-based camera. Due to the finite depth-of-focus, some areas of the volume will be in focus, and some will be blurred. Depth-by-defocus methods scan the focus through the volume and separate the contributions of sources at various depths. However, this limits depth resolution to that achievable by a single, stationary aperture. If the aperture is small enough such that the volume is completely within focus, then the camera can be laterally scanned to produce a tomographic reconstruction of the volume [26]. This permits more depth resolution, but limits the source size. Coherence-based techniques can effectively achieve a large depth-of-field by sampling the mutual intensity. The Van Cittert-Zernike theorem gives the relationship between the mutual intensity and the source power density, and demonstrates how coherence imaging achieves a large depth-of-field. The theorem states that the sampled mutual intensity in the Fresnel zone $J(\Delta x, \Delta y)$ of two points on a plane, separated by a displacement $(\Delta x, \Delta y)$, is the two-dimensional Fourier transform of the power density distribution of a planar source $I(x, y)$ located at a distance z from the sampling plane:

$$J(\Delta x, \Delta y) = \int_s \frac{I(x, y)}{4\pi z^2} \exp[-j\frac{2\pi}{\lambda}(\frac{x}{z}\Delta x + \frac{y}{z}\Delta y)]dxdy$$

If the source is now a volume source, then the contributions to the mutual intensity are summed over the volume, but points in the volume that have a constant x/z and y/z all contribute identically (except for an amplitude factor) to the mutual intensity $J(\Delta x, \Delta y)$. $J(\Delta x, \Delta y)$ represents the Fourier transform of the linear projections of the source with constant x/z and y/z, which is the in-focus version of the source for all depths where the Fresnel approximation applies. Tomographic methods can be applied to reconstruct the power density of its source from the projections. Since a three-dimensional set of projections is needed to recover a three-dimensional source, the mutual intensity will need to be sampled around many positions.

To measure the coherence function, we utilize a Rotational Shearing Interferometer, shown in Figure 47. It consists of a beamsplitter, two folding mirrors, and a focal plane array. The beamsplitter creates two identical wavefronts, which are rotated about the optical axis independently by the folding mirrors. The rotated wavefronts, when recombined by the beamsplitter, produce interference between field points with various separations $(\Delta x, \Delta y)$. The mutual intensity is sampled on the focal plane as a modulation on a constant background intensity. An interference filter is added in front of the focal plane to make the field quasi-monochromatic. To demonstrate depth-invariance, we imaged two transparent rulers, one of which was 30 cm from the pupil plane, the other over a meter away. Figure 48 shows that while the defocus is very large, the text on both rulers is clearly legible. A reconstruction of four light emitting diodes situated in three-dimensions is shown in Figure 49. To produce this image, the RSI was stepped to 256 positions 193 μm apart, and the two-dimensional mutual intensity was sampled at each position. The projections were recombined with a method very similar to that of

[26]. As these demonstrations show, RSI coherence imaging can reconstruct three-dimensional sources, and have the high depth-of-field property necessary for three-dimensional reconstructions over extended volumes.
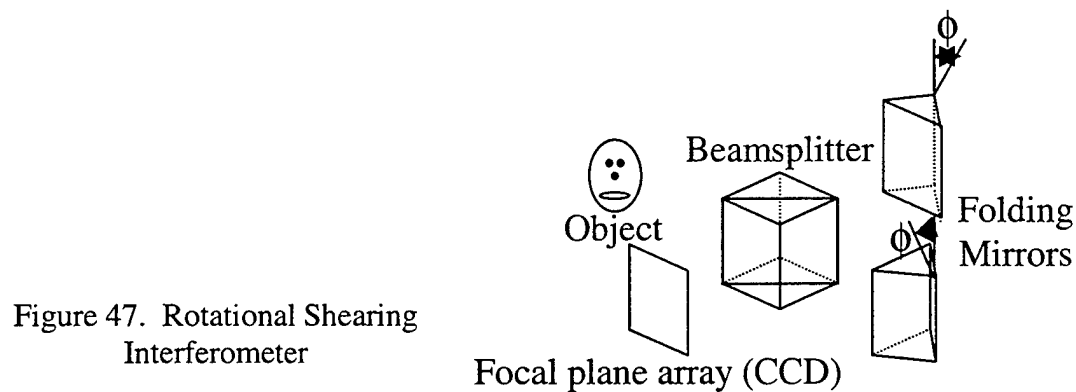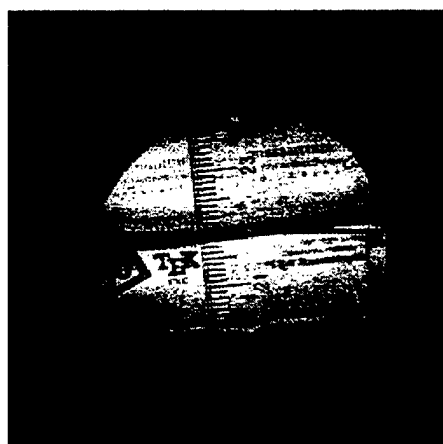

Figure 47. Rotational Shearing Interferometer

Figure 48. Two-dimensional RSI image showing depth invariance.

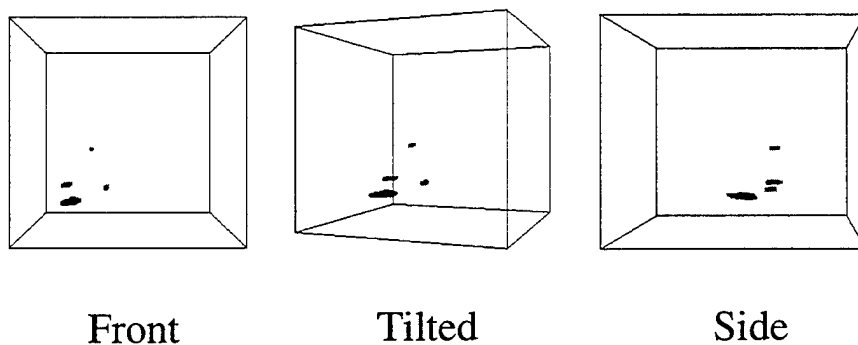

Front   Tilted   Side

Figure 49. Three views of a three-dimensional reconstruction of a four LED source sampled with a RSI.

Charge Coupled Device (CCD) cameras are the "digital film" which allow optical image data to be quickly captured and computationally enhanced. CCDs are being replaced in some applications by CMOS (complementary metal oxide semiconductor) APS (active pixel) sensors, which rely on standard VLSI processing and are potentially much cheaper than CCDs. For computational imaging APS sensors also offer advantages in that logic and filters can be integrated on the sensor plane and localized patches of the sensor can be read-out for optimal processing.

Bandpass filtering provides a particular example of APS sensors for digital imaging. In serial spectrometers, such as Fourier transform infrared (FTIR) systems, interference terms are filtered out by continuous analysis of a temporal signal. This approach greatly reduces mechanical stability requirements and data recording times in these systems. Sensor level filtering has not been possible in imaging systems because pixel data is read-out under a frame-based freeze and hold protocol to keep the sensor bandwidth reasonable. This limitation can be overcome using CMOS sensors by integrating bandpass filters at the pixel level before the freeze and hold layer. In this program we propose to use CMOS foundry services to produce suitable bandpass cameras.

In the near term interferometric imaging for ultrafast and data-fusion applications must implement processing roles into commercially available focal planes. One of the advantages of information-oriented optical design is that the focal plane can be modulated and moving during data acquisition. Distortions from motion are removed computationally. As an example of computation at the sensor level, we consider continuous non-frame based acquisition of coherence data using a CCD.

To understand the potential for focal plane processing, consider the cross-spectral density due to an incoherent source:

$$W\left(r_1, r_2, \omega\right) = \int \frac{I(r, \omega)}{|r - r_1||r - r_2|} e^{j\frac{\omega}{c}|r - r_1|} e^{-j\frac{\omega}{c}|r - r_2|} d^3 r$$

We then make some approximations:

$$R_1 \approx \frac{(x - \hat{x} + \Delta x)^2 + (y - \hat{y} + \Delta y)^2}{2(z + \Delta z)} + (z + \Delta z)$$

$$R_1 \approx \frac{(x - \hat{x} - \Delta x)^2 + (y - \hat{y} - \Delta y)^2}{2(z + \Delta z)} + (z + \Delta z)$$

to obtain

$$W(\hat{x}, \Delta x, \hat{y}, \Delta y, \Delta z, \omega) = e^{j\frac{2\omega}{c}\Delta z} \int \frac{I(r,\omega)}{4(z^2 - \Delta z^2)} e^{j\frac{\omega}{c}\frac{(x-\hat{x}+\Delta x)^2 + (y-\hat{y}+\Delta y)^2}{2(z+\Delta z)}} e^{-j\frac{\omega}{c}\frac{(x-\hat{x}-\Delta x)^2 + (y-\hat{y}-\Delta y)^2}{2(z-\Delta z)}} d^3r.$$

For the monochromatic case, assume $\Delta z = 0$. Then

$$W(\Delta x, \Delta y, q, \omega) = \int \frac{I(r,\omega)}{4z^2} e^{j\frac{\omega(x\Delta x + y\Delta y - q)}{c}} d^3r$$

where $q = \hat{x}\Delta x + \hat{y}\Delta y$.

Let x_f, y_f represent position in the local focal plane coordinates and suppose that x_g is the focal plane center position in global coordinates. Folding mirrors on each arm of an RSI retroreflect two fields for interference. The fold axis of one arm makes an angle θ with respect to the x axis. The fold axis of the other arm makes an angle $-\theta$. Then

$$\Delta x = 2 y_f \sin(2\theta)$$
$$\Delta y = 2 x_f \sin(2\theta)$$

and, in focal plane coordinates,

$$\hat{x} = 2 x_f \cos(2\theta)$$
$$\hat{y} = -2 y_f \cos(2\theta)$$

In the simplest case, the temporal signal leaving the row of the CCD at x_f is

$$S(x_f, t) = \sum_{n=0}^{N} W\left(\Delta x = 2 n p_f \sin(2\theta), \Delta y = 2 x_f \sin(2\theta), q(t - n\Delta), \omega\right)$$

$$= \sum_{n=0}^{N} \int \frac{I(r,\omega)}{4z^2} e^{j\frac{\omega(2xnp_f \sin(2\theta) + 2yx_f \sin(2\theta) - q(t-n\Delta))}{c}} d^3r$$

where p_f is the focal plane pixel spacing, Δ is the pixel integration time. Suppose that the center of the focal plane moves with velocity v such that $\hat{x} = 2 x_f \cos(2\theta) + vt$. Then

$$q(t - n\Delta) = 2(2 x_f \cos(2\theta) + v(t - n\Delta)) n p_f \sin(2\theta) - 4 n p_f x_f \cos(2\theta)\sin(2\theta)$$
$$= 2v(t - n\Delta) n p_f \sin(2\theta)$$

and

$$S(x_f, t) = \sum_{n=0}^{N} \int \frac{I(r,\omega)}{4z^2} e^{j\frac{2\omega}{cz}\sin(2\theta)\left(xnp_f + yx_f - v(t-n\Delta)np_f\right)} d^3r.$$

Letting $I_p(\bar{r}) = \frac{I(\bar{r},\omega)}{4z^2}$, $x' = \frac{\omega x}{\pi c z}\sin(2\theta)$, $y' = \frac{\omega y}{\pi c z}\sin(2\theta)$, $z' = \frac{\omega p_f}{\pi c z}\sin(2\theta)$, $t' = vt$, and $\Delta' = v\Delta$ and dropping the prime markings we obtain

$$S(x_f,t) = \sum_{n=0}^{N} \int I(\vec{r})e^{j2\pi\left(nxp_f + yx_f - (t-n\Delta)nz\right)}d^3r$$

Take a temporal and spatial Fourier transform of S

$$S(f_{x_f},v) = \sum_{n=0}^{N} \int I(\vec{r})\delta\left(f_{x_f} - y\right)\delta(v - nz)e^{j2\pi\left(nxp_f + n^2\Delta z\right)}d^3r$$
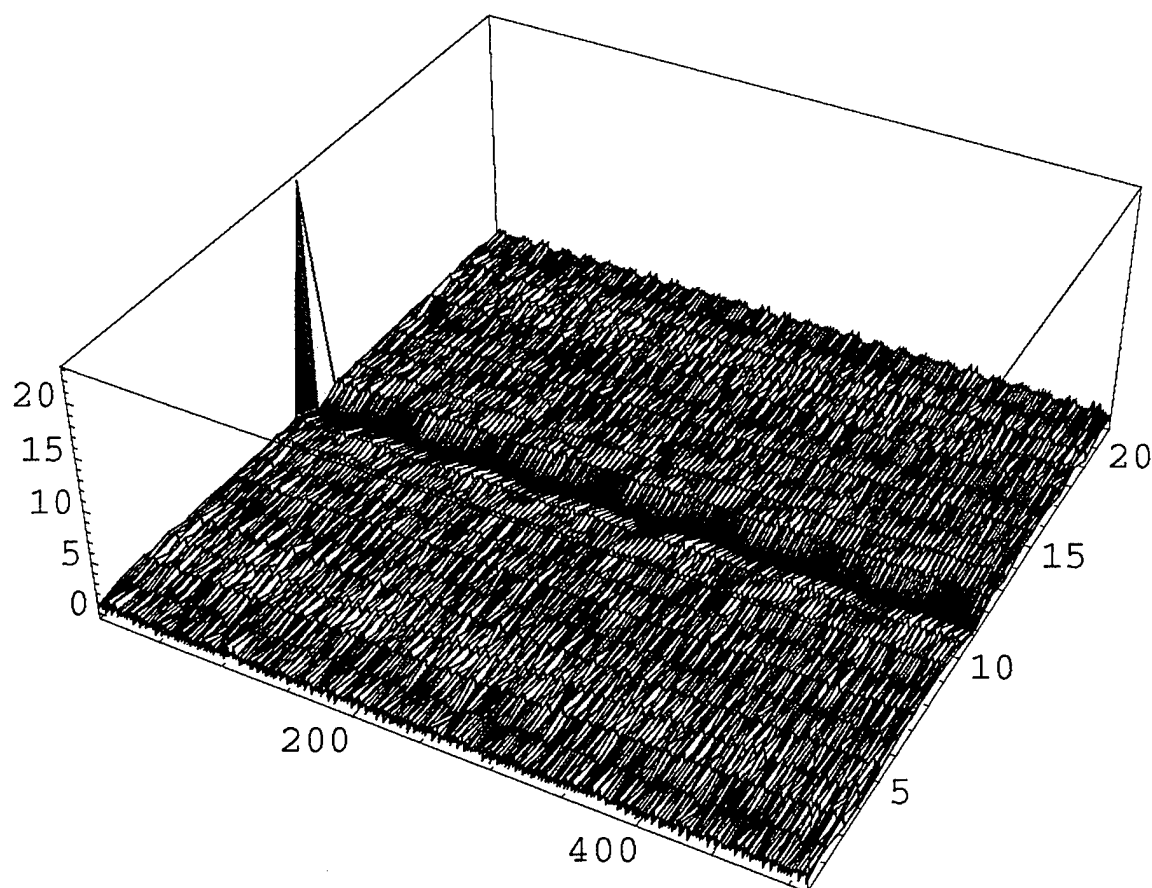
and filter with the "matched filter" $e^{-j\pi\alpha v^2}$. Taking the inverse temporal transform, we obtain

$$Q\left(f_{x_f},t,\alpha\right) = \int I(\vec{r})\delta\left(f_{x_f} - y\right)\sum_{n=0}^{N} e^{-j2\pi n\left(tz-xp_f\right)}e^{-j2\pi n^2\left(\frac{\alpha}{2}z^2-\Delta z\right)}d^3r$$

The plot below shows the sum as a function α on the rough axis and $tz - xp_f$ on the fine axis. The range of α is 0 to $4\Delta^2$. The range of $tz - xp_f$ is 0 to 1. The delta function is at $z = \dfrac{2\Delta}{\alpha}$ and

$x = \dfrac{2\Delta t}{p_f\alpha}$. On the basis of this inversion, we see that $Q\left(f_{x_f},t,\alpha\right) \approx I\left(x = \dfrac{2\Delta t}{p_f\alpha}, y = f_{x_f}, z = \dfrac{2\Delta}{\alpha}\right)$.

As this example indicates, a variety of processing functions can be integrated into the focal plane. This integration is essential to maximizing the data throughput of the sensor. As discussed above, obtaining the optimal balance between processing functions distributed in the optics, the focal plane, and digital hardware in is the primary goal of interferometric systems.

We have shown that novel and powerful distributed processing functions can be integrated into optical systems and focal planes. This section addresses the question: *How does this new functionality impact imaging systems?* The key change is that optical imaging becomes increasingly similar to modern 3D methods such as x-ray tomography, radio astronomy and magnetic resonance imaging. As in these cases, one uses distributed processing to produce computational models. The models need not be similar in appearance to focal plane data. Unlike a hologram, which captures a visually rich but still planar projection of an object, computational models are reconstructed in the full dimensional space of the object. In the case of

polychromatic, time varying or polarized objects, this space may include four or more dimensions.

As an example of computational imaging from distributed sensor data, we consider the application of x-ray transform algorithms to the visible spectral range. Tomography is a useful tool at optical wavelengths because we have systems that can measure projections through the source volume. A linear projection of an incoherent, nonscattering source would ideally be the linear sum of the power density of the source along lines through the source. A lens-aperture imaging system provides projections of these sources, as long as the source is confined to the depth-of-field region of the lens system, where the object is sharply in focus. Of course an RSI imager, with the essentially infinite depth of field illustrated in figure 48, measures projections for all visible source depths. In both cases, the projections will intersect through the center of the principal plane of the imager, forming a "cone" of projections from the principal plane. Because the projections are gathered in sets of cones, cone-beam tomographic algorithms are convenient to use to approximately invert the Radon transform. However, because the sources of interest are typically not incoherent or nonscattering, nonideal features will be introduced into the reconstruction.

The most essential differences between projective tomography in the visible and IR (VIR) and x-ray tomography are: VIR sources and objects tend to be opaque, VIR objects are often self luminous or ambiently illuminated, 2D electronic focal planes are more generally available in the VIR, and exposure restrictions are weaker in the VIR. Opacity is the only difference to impact image reconstruction algorithms. While opacity is also an issue in x-ray tomography, most studies have focused on reconstruction of volume densities in the neighborhood of dense obstructions. In VIR applications, the obstruction itself is often the object to be reconstructed. Several authors have considered reconstruction of dense obstructions from silhouette projections, but to our knowledge none have considered direct application of cone beam algorithms to the reconstruction of opaque objects.

It is surprisingly easy to account for opacity in the x-ray reconstruction of convex objects. For a convex object, opacity windows the range of angles over which projections through a given surface patch are observed. It can be shown that this angular window produces an angular window in the Fourier space of the object. The Fourier transform of this window is convolved with the surface density of the object on reconstruction. Since the patch impulse response, oriented normal to the surface, is associated reconstructed surfaces, estimation of surface positions is relatively straight forward.

Figure 51. Photograph of object.

Figure 52. RSI reconstruction.

Figures 51-55 shows results from 3D tomographic reconstruction using visible light. Figure 5 is a photo of a "Care Bear" figurine. Figure 52 is an interferometric RSI
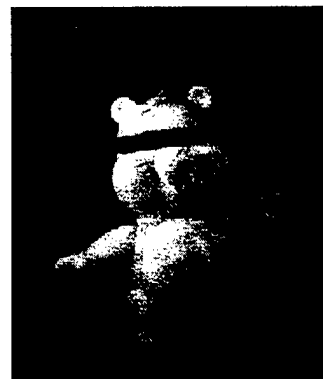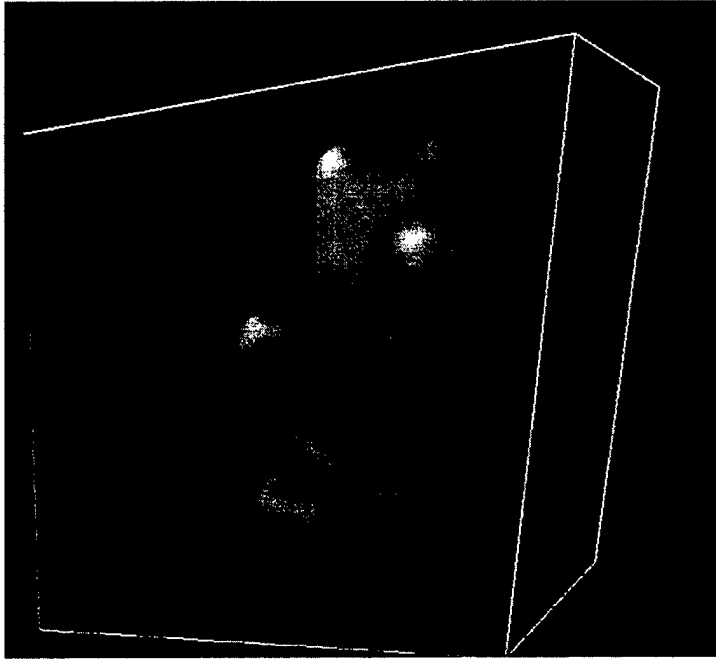
Figure 53. Projection of 128x128x128 cone-beam reconstruction.

reconstruction of the same object. The object was illuminated with incoherent fluorescent light for the RSI reconstruction. Figures 53 and 54 show projections cone-beam tomographic reconstructions of the bear. The 3D data set was constructed using a conventional camera with data from 128 perspectives. Figures 7 and 8 are volume renderings of the 128 by 128 by 128 data set from different perspectives. Because showing the linear projections of the reconstruction is really the inverse operation of the tomographic algorithm, this is expected to appear like the original object, except for obscuration, on the circle path over which the original data was taken. Because the object can be shown from angles and positions where the object was not originally imaged, more information about the object's true shape can be obtained. The reconstructions were formed using the cone-beam reconstruction algorithm of Feldkamp *et al.* [27].

As mentioned above, the impact of using tomographic reconstruction on projection data from convex opaque objects is a convolution of the reconstruction of the equivalent transparent surface with an impulse response. The impulse response is similar to a dipole field normal to the surface. As with a dipole field, one can estimate the driving charge, which in this case is the surface, by taking the Laplacian of the reconstructed volume data. This is illustrated in figure 55, which shows a cross-section of the 3D cone beam
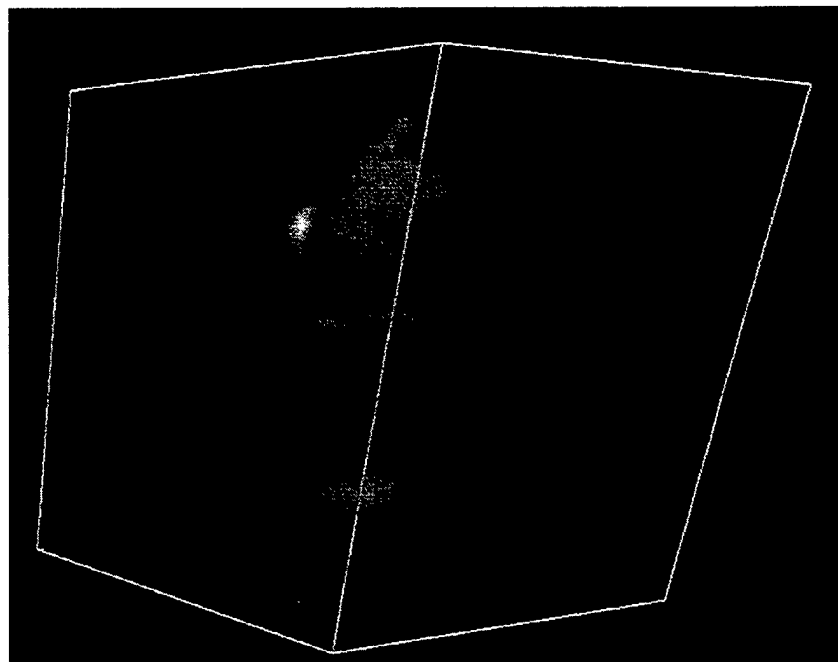

Figure 54. Projection of 128x128x128 cone-beam reconstruction.

reconstruction of an ambiently illuminated figurine and a cross-section of the Laplacian of the reconstruction. The surface shell is evident in the Laplacian data.

Feldkamp's algorithm is intended to reconstruct objects from which projections have been gathered in sets of cones, where the path of the points through which the projections have been gathered (the vertex path) is a circle. The algorithm is a filtered-backprojection type and can be considered an extension of the fan-beam reconstruction formula to three-dimensions. A circle vertex path does not provide sufficient data to reconstruct all points in the scene to full resolution; points that are further from the circle will reconstruct with less axial resolution. The Feldkamp algorithm is therefore an approximate formula because it can not perfectly reconstruct off-circle points. We chose this algorithm because it has sufficient reconstruction quality, is simple to implement, and has excellent computational performance compared to many other cone-beam tomographic reconstruction algorithms.

Cone beam reconstruction is a particular example of how multiple sensor data can be combined to create object models. Other examples include spatio-spectral-temporal reconstructions, polarization images, as well as other tomographic algorithms. In particular, several approaches may be considered to reducing the computational complexity of surface reconstruction. These revolutionary approaches to optical component, sensor and algorithm design are not a finished product, rather they suggest that new attention must be paid imaging system design for digital environments.
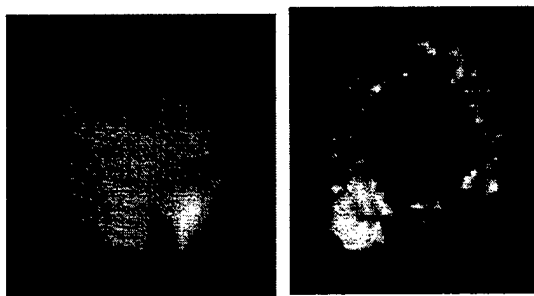

Figure 55. Cross-section of the cone-beam reconstruction of a figurine and the Laplacian of the reconstruction.

Conclusion

This program demonstrated:

1. That it is possible to build extra-ordinarily compact terahertz signal encoders using distributed bragg mirrors.
2. That emerging quantum dot materials technologies will yield point detectors capable of capturing and analyzing high information content ultra-broadband signals and
3. That interferometric characterization of complex space-time fields suggests radically new approaches to optical sensing and imaging.

These results suggest major new opportunities for ultra-fast communications and imaging. These opportunities are being pursued under new AFOSR, DARPA and ARO programs in collaboration with the Army Research Laboratory and other government and industrial collaborators.

References

1.	Froehly, C., B. Colombeau, and M. Vampouille, *Shaping and analysis of picosecond light pulses*, in *Progress in Optics*, E. Wolf, Editor. 1983, North-Holland Publishing Company: Amsterdam.
2.	Weiner, A.M., D.E. Leaird, and J.S. Patel, *Programmable femtosecond pulse shaping by use of a multielement liquid-crystal phase modulator.* Optics Letters, 1990. **15**: p. 326-328.
3.	Hillegas, C.W., et al., *Femtosecond laser pulse shaping by use of microsecond radio-frequency pulses.* Optics Letters, 1994. **19**(10): p. 737-739.
4.	Rebane, A. and J. Feinberg, *Time-resolved holography.* Nature, 1991. **351**: p. 378-380.
5.	Mazurenko, Y.T., *Holography of Wave Packets.* Appl. Phys. B, 1990. **50**: p. 101-114.
6.	Mazurenko, Y.T., et al., *Recording and reconstruction of femtosecond light pulses using volume holograms.* Optics Communications, 1993. **96**(4-6): p. 202-207.
7.	Acioli, L.H., et al., *Femtosecond temporal encoding in barium titanate.* Optics Letters, 1991. **16**(24): p. 1984-1986.
8.	Brady, D.J., G.S. Chen, and G. Rodriguez, *Volume holographic pulse shaping.* Optics Letters, 1992. **17**: p. 610-612.
9.	Hill, K. and D. Brady, *Pulse shaping in volume reflection holograms.* Optics Letters, 1993. **18**: p. 1739-1741.
10.	Hill, K. and David Brady, *Impulse responses of strong reflection holograms.* Applied Optics, 1993. **32**: p. 4305-4316.
11.	Hill, K.B., K.G. Purchase, and D.J. Brady, *Pulsed image generation and detection.* Optics Letters, 1995. **20**(10): p. 1201-1203.
12.	Brady, D. and D. Psaltis, *Information capacity of 3-D holographic data storage.* Optical and Quantum Electronics, 1993. **25**: p. S597-S610.
13.	Hill, K.B. and D.J. Brady, *Pulse shaping in volume reflection holograms.* Optics Letters, 1993. **18**: p. 1739-1741.
14.	Hill, K.B., et al., *Noise and information in interferometric cross correlators.* Applied Optics, 1997. **36**(17): p. 3948-3958.
15.	Purchase, K., D.J. Brady, and K. Wagner, *Time-of -flight cross-correlation on a detector array for ultrafast packet detection.* Optics Letters, 1993. **18**: p. 2129-2132.
16.	Purchase, K.G., et al., *The distributed Bragg pulse shaper.* submitted to the Journal of Lightwave Technology.
17.	Jimenez, J.L., et al., *The quantum dot spectrometer.* Applied Physics Letters, 1997. **71**(24): p. 3558-3560.
18.	Purchase, K.G., et al., *Dispersion compensation in coherence domain multiplexed systems.* Optics Letters, 1994. **19**: p. 1107-1109.
19.	Basinger, S.A., et al., *Superresolved optical scanning using polychromatic light.* submitted to Applied Optics, 1997.
20.	Basinger, S.A., D.J. Brady, and E. Michielssen, *Superresolution through space-time control of two-level quantum systems.* Journal of the Optical Society of America B, 1997. **14**(3): p. 503-510.

21.   Murty, M., *Interference between wavefronts rotated or reversed with respect to each other and its relation to spatial coherence.* Journal of the Optical Society of America, 1964. **54**: p. 1187-1190.

22.   Armitage, J.D. and A. Lohmann, *Rotary shearing interferometry.* Optica Acta, 1965. **12**: p. 185-192.

23.   Itoh, K., T. Inoue, and Y. Ichioka, *Interferometric spectral imaging and optical three-dimensional Fourier transformation.* Japanese Journal of Applied Physics, 1990. **29**(8): p. L 1561- L 1564.

24.   Roddier, F., *Rotation-shearing interferometry.* Proc. IAU Coll. 50 [C2], 1979.

25.   Roddier, C. and F. Roddier, *Imaging with a coherence interferometer in optical astronomy.* Proc. IAU Coll. 49 [C1], 1979: p. 175-179.

26.   Marks, D.L. and D.J. Brady, *Three-dimensional source reconstruction with a scanned pinhole camera.* Optics Letters, 1998. **23**(11): p. 820-822.

27.   Feldkamp, L.A., L.C. Davis, and J.W. Kress, *Practical cone-beam algorithm.* Journal of the Optical Society of America A, 1984. **1**: p. 612-619.